Materials & Design 270 (2026) 116860

Contents lists available at ScienceDirect

Materials & Design

journal homepage: www.elsevier.com/locate/matdes

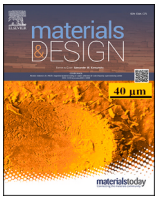

Hydrogel particles under uniaxial compression: Tetrapod-based DEM approach and experimental validation

Lara Gibowsky[a,b,1], Lukas Maier[c,1], Nanning Jaeschke[a], Irina Smirnova[a,b], Stefan Radl[c,*], Pavel Gurikov[a,b,d,**]

[a] Hamburg University of Technology, Institute of Thermal Separation Processes, Eissendorfer Str. 38, Hamburg, 21073, Germany
[b] United Nations University Hub on Engineering to Face Climate Change at the Hamburg University of Technology, United Nations University Institute for Water, Environment and Health (UNU-INWEH), Hamburg, 21073, Germany
[c] Graz University of Technology, Institute of Process and Particle Engineering, Inffeldgasse 13/III, Graz, 8010, Austria
[d] Aerogel-It GmbH, Albert-Einstein Str. 1, Osnabrück, 49076, Germany

HIGHLIGHTS

- Elastic limit of biopolymer-based hydrogels under uniaxial compression identified ($\epsilon \approx 0.5$).
- Viscoelastic apparent strain-stiffening regime revealed that is rate-independent beyond a characteristic piston speed ($\approx$ 0.5 mm/s).
- Biphasic tetrapod DEM-based model (polymer network and water) matches experimental force–strain response.
- Model validated on unseen experiments, confirming load-bearing tetrapod network, internal fluid redistribution, and extensibility to more complex polymer–solvent interactions.

ARTICLE INFO

Keywords:
DEM simulation
Tetrapods
Hydrogel mechanics
Uniaxial compression
Apparent Young's modulus
Experimental validation
Multiphysics simulation

ABSTRACT

Hydrogels are soft, water-rich polymer networks whose mechanical behavior governs applications ranging from biomedicine to packed bed processes. In aerogel manufacturing, hydrogel particles represent an intermediate state in which mechanical stability determines scalability and process reliability. However, predictive particle-scale models for deformable matrix-fluid systems remain limited. Biopolymer-based hydrogel particles are investigated under uniaxial compression through monotonic, cyclic, and stress-relaxation experiments at compression rates of 0.1–3.0 mm/s. Apparent stiffness increased strongly with rate, followed by saturation above 0.5 mm/s, where the apparent Young's modulus became rate independent. Within the elastic regime, the response is reproducible and hysteretic, whereas higher strains induced plastic deformation. Aging over one year led to additional stiffening, indicating ongoing structural evolution. To complement the experiments, a novel discrete-element-method framework based on tetrapod-shaped parcels is introduced. Tetrapods qualitatively represent the 3D polymer network and predominantly carry mechanical loads, while embedded spheres mimic the aqueous phase. Parameters are calibrated using a full-factorial design and Bayesian optimization. Simulations reproduce the force–strain response, apparent elastic properties, and particle deformation. Random packings produce comparable scatter, while stress relaxation and cyclic loading are reproduced qualitatively. The approach advances predictive modeling of deformable particles and provides a basis for solvent exchange and process-scale simulations.

* Corresponding author.
** Corresponding author at: Hamburg University of Technology, Institute of Thermal Separation Processes, Eissendorfer Str. 38, Hamburg, 21073, Germany.
Email addresses: lara.gibowsky@tuhh.de (L. Gibowsky), lukas.maier@tugraz.at (L. Maier), nanning.jaeschke@tuhh.de (N. Jaeschke), irina.smirnova@tuhh.de (I. Smirnova), radl@tugraz.at (S. Radl), pavel.gurikov@tuhh.de (P. Gurikov).

[1] These authors contributed equally and share first authorship.

https://doi.org/10.1016/j.matdes.2026.116860
Received 3 March 2026; Received in revised form 13 August 2026; Accepted 20 August 2026
Available online 26 August 2026

Abbreviations

ANOVA	Analysis of Variance
BET	Brunauer–Emmett–Teller
BPM	Bonded Particle Model
$CaCl_2$	Calcium chloride
CFD	Computational Fluid Dynamics
CG	Coarse-grain
CM	Continuum Models
CO_2	Carbon dioxide
DEM	Discrete Element Method
DPD	Dissipative Particle Dynamics
fcc	face-centered cubic
FEM	Finite Element Method
G/M	guluronic to mannuronic acid
GPR	Gaussian Process Regression
HPC	High-performance computing
IUPAC	International Union of Pure and Applied Chemistry
LBM	Lattice Boltzmann Method
MD	Molecular Dynamics
MESO-P	Meso-Particle Models
MP	multi-particle
N/A	Not available
PDF	Probability Density Function
RMSE	Root Mean Squared Error
RMSLE	Root Mean Squared Logarithmic Error
SDG	Sustainable Development Goal
SEM	Scanning Electron Microscopy
SPH	Smoothed-Particle Hydrodynamics
TAR_{30}	Transverse-to-axial ratio at 30% strain
UN	United Nations

Latin characters

$\mathbf{A}$	Particle contact area [m^2]
c_n	Viscous constant for normal contact [–]
c_{solid}	Solid content [–]
c_t	Viscous constant for tangential contact [–]
CV	Coefficient of variation [–]
D	Diameter of spheres constituting a tetrapod [m]
d	Mean hydrogel diameter [m]
$d_{eq,ij}$	Equilibrium distance between species i and j [m]
d_{ij}	Distance between species i and j [m]
$d_{max,ij}$	Maximum effective distance between species i and j [m]
e	Coefficient of restitution [–]
F	Force on upper mesh or probe [N]
$f(x_t)$	Objective value at iteration t [–]
F_{ij}	Force between species i and j [N]
$f(t)_{best}$	Best objective value up to time t [–]
$\mathbf{f}^C$	Contact forces [N]
$\mathbf{f}^{coh}$	Cohesive force [N]
$\mathbf{f}^f$	Fluid forces [N]
$\mathbf{f}_i$	Force on particle i [N]
$\mathbf{f}^{NC}$	Non-contact forces [N]
$\mathbf{f}_n^{el}$	Elastic normal forces [N]
$\mathbf{f}_n^{vis}$	Viscous normal forces [N]
g	Gravitational acceleration [m/s^2]
H	Displacement [m]
h_{ij}	Harmonic stiffness between species i and j [N/m]
$\mathbf{I}_i$	Moment of inertia of particle i [$kg\,m^2$]
k_{hz}	Hertzian stiffness [$N/m^{3/2}$]
k_t	Tangential stiffness [N/m]
m_i	Mass of particle i [kg]
p	p-value [–]
R	Radius of sphere [m]
r	Center-to-center distance [m]
$\mathbf{r}^*$	Normalized hydrogel radius [–]
R^2	Coefficient of determination [–]
$\mathbf{r}^C$	Effective contact radius [m]
$\mathbf{r}_{eff}$	Effective radius [m]
r_i	Radius of species i [m]
s_i	Sample standard deviation of distribution i [–]
$s_{eq,ij}$	Normalized equilibrium distance between species i and j [–]
s_{ij}	Normalized distance between species i and j [–]
s_{max}	Normalized maximum effective distance [–]
t	Time (or time step) [s]
$\mathbf{t}^*$	Other torques [N m]
$\mathbf{t}_i$	Torque on particle i [N m]
v	Compaction rate [m/s]
$\mathbf{v}_i$	Velocity of particle i [m/s]
w	Alginate weight fraction [wt.%]
w_i	Mass fraction of species i [–]
$\mathbf{x}_i$	Position of particle i [m]
Y	Young's modulus (simulations) [J/m^3]
Y^*_{app}	Reduced apparent Young's modulus [J/m^3]
Y_{app}	Apparent Young's modulus [J/m^3]

Greek characters

$\dot{\delta}_n$	Change of normal overlap [m/s]
δ_n	Normal overlap [m]
Δt	Relative improvement in time t [–]
μ_{rr}	Rolling friction coefficient [–]
μ_{rs}	Sliding friction coefficient [–]
ν	Poisson's ratio (simulations) [–]
ν_{app}	Apparent Poisson's ratio [–]
ω_i	Angular velocity of particle i [rad/s]
ϕ_p	Particle volume fraction [–]
ρ_i	Density of species i [kg/m^3]
ρ_{hydro}	Density of hydrogels [kg/m^3]
ρ_s	Skeleton density of alginate network [kg/m^3]
ρ_w	Density of water [kg/m^3]
ε	Strain [–]
ξ	Tetrapod radius [m]
ξ/D	Interlocking parameter (i.e., tetrapod radius to sphere diameter ratio) [–]
ζ	Numerical stability constant [–]

1. Introduction

1.1. Motivation

Hydrogels are versatile soft materials that offer cross-linked three-dimensional polymer networks with a high water content. Due to their inherent biocompatibility, tunable mechanical properties, and favorable transport characteristics, they are employed across a broad range of biomedical, pharmaceutical, and food science applications [33,36,63,66]. A more specialized application of liquid filled gels lies in their role as smart, stimuli-responsive components in reactor systems, for instance as self-regulating outlet elements. External stimuli can induce macroscopic changes in gel structure, such as swelling or shrinkage, which can be exploited to control adaptive valves within reactors [22,34]. Typical triggers encompass variations in temperature, pH, or solvent composition of the surrounding medium. These structural changes affect the elastic properties of gels, such as the Poisson's ratio and Young's

modulus [32], making their characterization and predictive modeling highly relevant for practical applications. The mechanical behavior of hydrogels directly governs their stability, processability, and functionality in practical applications [72]. In particular, their elasticity, deformation resistance, and viscoelastic response, largely dictated by crosslinking density, and polymer-solvent interactions, determine how hydrogels deform and recover under mechanical load.

Although hydrogels are often studied as single particles or bulk materials, their arrangement in packed bed configurations is highly relevant for process applications such as aerogel production. Aerogels are derived from liquid filled gels by replacing the liquid with a gas while preserving the intrinsic polymer network, through three stages: i) gelation to form the hydrogel, ii) solvent exchange (replacing water with an organic solvent), and iii) supercritical Carbon dioxide (CO_2) drying to obtain the final aerogel. These materials exhibit extremely high porosity (up to $\approx$ 99 %), very low density, and large specific surface areas, and were recognized by the IUPAC in 2022 as one of the Top 10 Emerging Technologies in Chemistry [27]. Commonly used in their particulate form, they facilitate easier handling and simplify the scalability of the production process, while millimeter-sized particles reduce diffusion limitations during solvent exchange and supercritical drying [68].

In this context, hydrogel particles represent a mechanically crucial intermediate stage in the application of packed beds in aerogel production. Hydrogels due to their soft and deformable nature require careful handling and therefore single-particle characterization provides a logical starting point for a multiscale understanding. Their deformation under load can influence bed structure and voidage thereby affecting pressure drop, mass transfer, process efficiency, and ultimately the quality of the final aerogel product. In extreme cases, excessive deformation may even contribute to local bed failure. Therefore, understanding the mechanical response of individual hydrogel particles is essential for the design and operation of packed-bed processes and provides the basis for linking particle-scale behavior to bed-scale performance under process-relevant conditions.

Basic uniaxial compression experiments offer direct insight into particle stability, enabling systematic evaluation of apparent elastic properties, large-deformation behavior, and the influence of compression rate, all crucial for scaling up from laboratory to pilot scale. In particular, packed-bed processing is closely linked to mechanical properties governed by the surrounding solvent, which evolve continuously throughout the production route. While the present work does not reproduce the full complexity of packed-bed operation, it establishes the single-particle mechanical basis required for future multiscale investigations of particle assemblies and bed behavior. Despite this relevance, the mechanical aspects of this process have so far received little attention and remain largely unexplored. More broadly, many other applications also depend on the deformable nature of biomass or soft particles within fixed beds. For example, during the hydrolysis of straw, excessive deformation can lead to flow blockages in the bed [59]. Related particle-based processes extend far beyond aerogel production and include catalytic reactors, chromatography, fluidized beds, etc., showing a high dependency on the properties of the single particle system. [10,20,39].

To address these mechanical challenges of multi-particle applications computationally, the experimental study is complemented with coarse-grained Discrete Element Method (DEM) modeling, to gain deeper insight into hydrogel particle behavior under compression. The following literature review highlights the advantages and strengths of DEM compared to other mechanical simulation methods (summarized in Table A-1). Therefore, this work focuses on the investigation of the potential of an innovative and relatively unexplored particle geometry: tetrapods, which are multi-sphere parcels consisting of four distinct spheres that are rigidly connected via intra-parcel bonds. This geometry enables representation of the 3D hydrogel architecture by modeling a general porous polymer network with enclosed spherical meso-particles that mimic the aqueous phase of the gel. Thus, a biphasic simulation framework is established in which compressive loads are primarily absorbed by the tetrapods (i.e., the polymer network) rather than by the aqueous phase, making them the load-bearing structural component. Overall, the ultimate goal is to predict the experimental mechanical behavior of gels in packed beds from simulations. With that in mind, this approach supports UN SDG 9 by enabling the optimization of particle-based processes and SDG 12 by minimizing the extent of required experimentation.

1.2. Literature review - modeling

To place the proposed tetrapod-based modeling approach in the context of existing numerical strategies, the following section reviews established methods for simulating the mechanical behavior of hydrogels and soft polymer networks. Particular emphasis is placed on particle- and molecule-resolved approaches, highlighting their capabilities and limitations for soft and highly deformable systems. A summary of the features, application scales, advantages, and drawbacks of each method is shown in Table A-1.

1.2.1. Atomistic models

Atomistic models attempt to represent structures by directly modeling their molecules. Several researchers have particularly used Molecular Dynamics (MD)-based models and similar approaches to study how hydrogels behave mechanically.

Li et al. [45] made a valuable contribution by reviewing how MD helps to understand the structure of a hydrogel and its mechanical behavior. Lei et al. [43] took this further by exploring different network modeling approaches, including MD, coarse-grained MD, and abstract models for hydrogels. The computational expense of all these models becomes extreme when determining the mechanical properties of millimeter-sized particles or packed beds. To circumvent these computational challenges, Lei et al. [44] and Nikolov [52] adapted coarse-grain (CG) bead-spring models for hydrogels using Dissipative Particle Dynamics (DPD). This approach enables running longer simulations and handling larger systems compared to traditional MD. Nevertheless, scaling up to millimeter-sized particles is still a challenge. Liu et al. [46] also studied how physical and chemical crosslinking interact in hydrogels using atomistic models, showing how these interactions control mechanical strength and elasticity. In summary, atomistic models, use highly accurate interactions at high resolution to capture microscopic behavior. However, they are constrained to atomic scales and require large computational resources. Consequently, applying these methods to model macroscopic experimental systems remains impractical for millimeter-sized particles or multi-particle systems.

1.2.2. Meso-particle models (MESO-P)

MESO-P models, particularly those employing DEM-based methodologies, have emerged as a prominent computational framework for investigating hydrogel particle mechanics. These approaches achieve a balance between computational efficiency and physical fidelity by using coarse-grained representations of inter-particle forces, thus enabling the simulation of larger-scale systems while preserving essential mechanical characteristics. Bridging the gap between atomistic and continuum scales, Johnson et al. [38] introduce an intermediate approach that employs Brownian dynamics to capture the stochastic thermal motion and colloidal-scale interactions of particles suspended in a viscous medium. This work focuses on bond strength and network morphology affecting viscoelasticity, offering insight into the interplay between microstructure and rheology. However, such colloidal-scale modeling still requires substantial computational resources. Alternative meshless methods such as Smoothed-particle hydrodynamics (SPH) have also been explored for soft matter systems. For instance, Castro and Radl [13] applied SPH to simulate extremely deformed granular packings, demonstrating its capability to capture large deformations without the mesh constraints typical of continuum approaches.

Several distinct DEM-based approaches have been developed for hydrogel applications. Mascara et al. [49] employ a DEM-Bonded Particle

Model (BPM) with generalized Maxwell equations for viscoelastic behavior prediction, while Yang et al. [76] use a similar approach for fracture analysis in hydrogel monoliths. Depta et al. [18] develop bonded DEM formulations for alginate gelation kinetics using Langevin dynamics principles. Furthermore, solvent-free aerogels as representations of single-phase polymer networks with reduced complexity were investigated with the DEM-BPM model in cylindrical geometry by Dosta et al. [21] and in small packed bed arrangements by Alves et al. [2]. Classical DEM approaches that model strongly deformed macro particles have been explored by Zunker et al. [84], who implemented a complex contact mechanics framework. However, classical DEM approaches do not capture intra-particle phenomena such as particle deformation, or liquid transport within a gel. Both aspects are considered to be critical for the prediction of hydrogel behavior. In contrast to such rigid-particle approaches, Haustein et al. [29] and Rojek et al. [62] developed deformable discrete element methods that allow individual spheres to change shape during contact—using radial expansion techniques and three-dimensional extensions, respectively, to capture large-deformation behavior. Classical BPM approaches require the evaluation of numerous inter-particle bonds at each time step, necessitating the availability of large computational resources. The tetrapod modeling approach offers a potentially more efficient alternative by replacing explicit bonding with cohesive interactions between parcels, while still enabling selective load-bearing by a distinct network phase. Additionally, tetrapods enable the construction of an extremely porous structure, that allows the placement of water meso-particles within—similar to what constitutes a gel. This novel computational methodology, proposed in the present study, remains relatively unexplored within the scientific literature. Initial publications by Radl et al. [57] and Maier et al. [48] establish the foundational framework for tetrapod-based particle modeling applications.

In summary, MESO-P models offer computational efficiency advantages over atomistic approaches while maintaining essential mechanical characteristics. However, parameter calibration remains challenging, and accurate representation of fluid migration presents ongoing limitations. Nevertheless, these methods enable practical simulations of millimeter-sized particles and larger systems.

1.2.3. Continuum models (CM)

CM, most commonly implemented via the Finite Element Method (FEM), offers a scalable and flexible framework for modeling hydrogel mechanics, overcoming the system-size limitations inherent to atomistic methods. However, conventional FEM approaches face notable constraints, including their inability to capture fracture phenomena, free water transport, and atomic-scale resolution [8].

For hydrogels undergoing large swelling, diffusion-deformation models are widely employed, coupling time-dependent chemical potential and mechanical displacement fields to describe network swelling behavior [1,74]. Several studies have adopted a continuum modeling framework to investigate soft, deformable hydrogels. Czerner et al. [17] implemented indentation-based FEM to determine the Young's modulus of gelatin gels, while Aygün and Klinge [5] presented a multiscale FEM-based model, successfully predicting the mechanical behavior of biphasic, ultrastable hydrogels reinforced with calcified microstructures. In contrast, Nguyen et al. [51] applied a single-scale FEM approach incorporating a poroelastic and linear viscoelastic material model while assuming negligible water loss. Their model successfully simulated the force-displacement behavior of alginate microspheres under compression and subsequent relaxation.

Further extending poroelastic modeling, Cai et al. [9] investigated the compression of alginate hydrogels while extracting both elastic and transport properties predicting long relaxation times (i.e., 3 h to 8 h) and revealing inhomogeneities in solvent concentration. More recently, Zeng et al. [78] coupled Computational Fluid Dynamics (CFD) with FEM to simulate hydrodynamic loading of spherical hydrogel particles within a fluid-filled channel, resolving the pressure and velocity distribution and determining apparent Young's moduli.

To model large ensembles of interacting deformable particles, multi-particle (MP)-FEM combines the advantages of CM and DEM by treating each particle as a fully meshed continuum body. Loidolt et al [47] and Zunker et al. [84] successfully applied this approach to simulate the compaction of powders consisting of an elasto-plastic material, capturing large-deformation behavior. Recently, Castillo-Acuna and Kochmann [12] proposed a maximum-entropy meshless framework coupling solvent diffusion with large-strain mechanical deformation on a point-cloud discretization, enabling robust modeling of extreme volumetric changes and geometric instabilities where conventional meshes fail. This approach remains a continuum model, in contrast to meso-scale particle-based methods such as DEM, or SPH, solved with a meshless maximum-entropy scheme.

In summary, CM approaches provide scalable frameworks for simulating hydrogel mechanics, including swelling, visco- and poroelastic transport, though they are limited in capturing fracture and nanoscale effects. Recent advances, such as multiscale and multi-particle FEM, have enhanced predictive capabilities by integrating structural heterogeneity and large deformation behavior. Despite these advancements, such continuum frameworks are often complex to implement, and their application to large-scale multi-particle systems remains computationally prohibitive and hence often not feasible (compare Table A-1).

1.3. Literature review - elastic properties of hydrogels under compression

Hydrogels are widely used as carrier matrices in food, medical, and enzyme immobilization applications, where their mechanical properties ensure structural integrity and prevent mechanical failure [66]. In particular, parameters within elastic deformation under compressive loading, such as Young's modulus and Poisson's ratio, are crucial for design and as input data for simulations. Biopolymer-based hydrogels typically exhibit elastic behavior up to compressive strains of 50 % [75]. While the mechanical characterization is typically performed on cylindrical monoliths due to their uniform stress distribution and reproducibility, assessing spherical particles remains challenging because of the time-dependent contact area during compression. Therefore, the Hertz theory is commonly applied, describing the compression of a linearly elastic solid sphere between two flat surfaces and enabling the determination of the Young's modulus [31].

The Young's modulus is commonly defined as the intrinsic elastic constant of the polymer network, valid in the low-strain regime up to about 5–10% strain [14,25,75]. By contrast, the apparent Young's modulus and apparent Poisson's ratio may vary with strain rate because they characterize the response of the coupled polymer matrix-fluid system. These parameters should therefore be interpreted as apparent, rate-dependent quantities that reflect the combined mechanical and fluid-transport response and are primarily useful for comparison between test conditions. The apparent Young's modulus of biopolymer-based hydrogels is within the range of 1 kPa to 1000 kPa, highly dependent on polymer network characteristics (concentration, cross-linking density, and gelation conditions), macroscopic shape, compression rate, as well as fluid transport [6,75,79]. In the case of alginate-based hydrogels Chan et al. [14] reported apparent Young's moduli ranging from 200 kPa to 650 kPa, while lower values below 100 kPa were observed by Ouwerx et al. [54]; more recently, Apuu et al. [3] determined comparable moduli for alginate hydrogels using a nondestructive, actuator-based method. However, the compression rate significantly alters the coupled mechanical and fluid flow response of hydrogels. This time-dependent effect is attributed to (i) the intrinsic viscoelastic properties of the biopolymer network and (ii) the dynamics of water transport within and outside of the gel matrix [24,75,80]. Wang et al. [75] suggest that force response and corresponding apparent Young's modulus reach a plateau at a high deformation rate of $\approx$ 36 mm/min, indicating a transition towards a rate-independent behavior for high rates [73]. Additionally,

Ed-Daoui and Snabre [24] revealed that both apparent Poisson's ratio and apparent Young's modulus decrease at lower loading rates, due to better fluid redistribution and delayed structural rearrangement. Poisson's ratios in the range 0.47 to 0.50 were reported with about 0.31 for alginate-based hydrogels [24,51]. In general, there are only very few studies available that examine all mechanical properties for one system (apparent Young's modulus, apparent Poisson ratio, shape) necessary as input for physically grounded simulations.

Hydrogels are widely recognized for their high water content, typically exceeding $90\,\%$, which influences the mechanical behavior of hydrogels. As compressive strain increases, the contribution of water to the overall stress becomes more pronounced, eventually surpassing that of the polymer matrix. In contrast, the hydrogel volume decreases as a result of water loss, especially during plastic, irreversible deformation [14,75,79].

More detailed insights into the time-dependent relaxation behavior within the elastic deformation of microspheres were provided by Zhao and Zang [80] and Wang et al. [75]. They suggested that the relaxation of forces during this phase might be attributed to water loss and the viscoelastic nature of the hydrogel showing shorter relaxation times at higher compression rates.

However, existing studies rarely address the aging behavior or batch-to-batch reproducibility of biopolymer-based hydrogels. Although studies report pronounced mechanical weakening due to progressive Ca^{2+} crosslinking loss or rapid stiffening within the first two weeks [4,15,42], no long-term studies spanning several months are available.

1.4. Knowledge gaps

Although DEM approaches have significantly advanced the understanding of hydrogel mechanics, several knowledge gaps remain that currently limit their predictive capabilities and transferability. These include the lack of physically grounded parameterization, limited capability to represent heterogeneous polymer network structures, insufficient treatment of time-dependent mechanical behavior, and insufficient treatment of solid-fluid phase coupling in highly deformable biphasic systems. Addressing these gaps is essential for developing predictive models that can be transferred across length scales and processing conditions.

In this work, a novel tetrapod-based particle model is investigated as an alternative DEM approach to commonly used representations of hydrogel networks. Within the multisphere-parcel framework, each tetrapod consists of multiple distinct spheres combined into a single parcel, such that the equation of motion is solved once per parcel. Unlike conventional DEM or BPM-DEM approaches, this method allows mechanical load transmission through a simplified network representation rather than through entire meso-particles. To date, this methodology has not been extended to deformable systems such as hydrogels. The present framework introduces an explicit mechanical coupling between the solid tetrapod network and the interstitial water meso-particles through a cohesive force model, constituting a biphasic representation in the spirit of established solid-fluid coupling frameworks [26,50]. While a fully resolved, physics-based biphasic treatment, capturing, for instance, poroelastic fluid flow and time-dependent pressure dissipation, remains an open challenge [69], the present approach establishes a clear pathway toward predictive process-scale simulations.

A further knowledge gap concerns the quantitative interpretation of DEM parameters in relation to experimentally accessible hydrogel properties. Although existing DEM approaches can reproduce qualitative deformation trends, their parameterization often lacks direct physical meaning. Specifically, the influence of network topology and geometry on macroscopic mechanical response remains insufficiently characterized and cannot be modeled with classical deterministic continuum models. The tetrapod model introduced here is explicitly a phenomenological representation: its parameters are calibrated to macroscopic experimental observables rather than derived from molecular quantities such as crosslinking density or polymer-solvent interaction parameters. This is a deliberate modeling choice, consistent with similar phenomenological approaches in the mechanics of network materials [58], and is motivated by the need for computational tractability at the scale of whole particles and particle beds. Closing the gap between phenomenological parameters and physically grounded molecular quantities remains an important direction for future work. The tetrapod network framework enables mechanical load transmission carried primarily by the spring-based tetrapod network, while the aqueous meso-particle phase contributes indirectly through its cohesive coupling with the tetrapod network, governing the redistribution of the fluid phase under compression. This distinguishes the present approach from conventional BPM-DEM simulations, in which forces are transmitted through the entire primary particles.

Finally, our present study outlines a conceptual pathway for extending the present biphasic tetrapod model toward a transport-resolved solvent-exchange framework that distinguishes water and an organic solvent within the polymer network. Solvent exchange is known to alter hydrogel mechanical properties and density profoundly through the stepwise replacement of water confined within the three-dimensional polymer network by an organic solvent such as ethanol [19,83]. To the best of the authors' knowledge, the modeling of solvent exchange at the scale of millimeter-sized particles has not yet been investigated. Capturing these effects is essential for meaningful mechanical characterization, reliable scale-up, and robust process design. Incorporating an organic solvent into the simulation framework would enable new perspectives for modeling solvent exchange processes, transport phenomena, and ultimately the scale-up of (hydro-)gel multiparticle systems.

Although numerous experimental studies have examined the mechanical properties of hydrogels, only a few studies provide complete characterization of the mechanical, structural, and physical properties required as input parameters and for validation of the simulations. Furthermore, the long-term aging behavior of hydrogels has been studied only to a limited extent and therefore represents an additional knowledge gap.

1.5. Goals

Firstly, this work aims to investigate the mechanical behavior of alginate-based hydrogels under uniaxial compression as a representative soft deformable system, thereby seeking to establish an experimental basis required for the parametrization and validation of the model. This includes apparent elastic and viscoelastic responses (such as apparent Young's modulus, apparent Poisson's ratio, and relaxation behavior) as well as structural and physical properties (density, water content, outer shape during compression, etc.), analyzed as a function of the compression rate to assess time-dependent effects. Additionally, the aging behavior over the course of one year will be examined.

Secondly, a tetrapod framework will be developed and adapted to model highly deformable materials such as hydrogels for the first time. The DEM-based model will be calibrated using experimental force–strain data at a specific compression rate, while validation will be performed using data from complementary experiments conducted at different compression rates. To capture the biphasic nature of hydrogels, the model represents the porous polymer matrix by an interconnected network of tetrapods, while embedded meso-particles account for the aqueous phase within the network. The network generation will be based on physical properties of the real hydrogel (e.g., the water content) to ensure physical relevance, and simultaneously attempts to model the load-bearing role of the polymer network under compression. In addition, this biphasic DEM approach for hydrogels shall enable the systematic investigation of network topology and heterogeneity effects on the mechanical response under compression, thereby complementing recent findings by Maier et al. [48]. This modeling framework aims to contribute to reducing the knowledge gap between microscopic polymer network behavior and macroscopic mechanical response.

Based on these results, a general modeling framework may in the future be established that provides a foundation for extending the tetrapod approach to other solvent systems such as organic solvents introduced via stepwise solvent exchange, and to a broader range of soft, porous materials.

2. Methods

2.1. Experimental

2.1.1. Hydrogel sample preparation

The biopolymer-based hydrogels investigated in this work were prepared using sodium alginate with a guluronic to mannuronic acid (G/M) ratio of 0.57 (IFF Division Pharma Solutions). The alginate powder was initially dissolved with a concentration of 2 wt.% in deionized water under continuous stirring with an overhead stirrer for 2 h, followed by one hour of treatment in an ultrasonic bath to ensure complete homogenization of the solution. The resulting aqueous solution was stored at 4 °C overnight to maintain consistent conditions during the gelation and to eliminate air bubbles, thereby preventing structural defects such as voids in the biopolymer matrix.

The gelation process was performed by ionic crosslinking, using a 2 wt.% aqueous calcium chloride ($CaCl_2$) solution (Carl Roth GmbH & Co. KG) as the crosslinking agent. The alginate solution was dripped into a $CaCl_2$ bath using a spider dripping setup equipped with needles of 0.7 mm inner diameter, positioned 12.00 cm above the crosslinking bath. Afterwards the particles were stirred overnight in the $CaCl_2$ bath to ensure thorough gelation of the hydrogels. This method aims at the formation of homogeneous and spherical hydrogel particles with an average diameter of ≈ 2 mm. To prevent microbial contamination or aging of the samples, the hydrogel beads were stored in sealed containers filled with fresh deionized water in a fridge until the experiments were performed. In addition, small amounts of sodium azide (≤ 0.05 wt.%) were added to the deionized water solution in which the hydrogels were stored to prevent microbiological growth.

2.1.2. Sample characterization

The density of millimeter-sized hydrogel particles is difficult to access precisely due to the geometric limitations of spheres such as non ideal sphericity. Thus, the density was calculated based on Eq. (1).

$$\rho_{hydro} = \left(\frac{c_s}{\rho_s} + \frac{1 - c_s}{\rho_w} \right)^{-1} \tag{1}$$

The solid content c_s (given in $g_{drymass}/g_{hydrogel}$) was determined by drying a ≈ 6.5 g hydrogel sample at 105 °C overnight. After the removal of water, the remaining component is the shrunken biopolymer network. The mass loss of the sample can then be used to determine the weight-related water and the solid content of the hydrogel. The measurement was performed in triplicate. Furthermore, the skeleton density ρ_s of dried alginate samples was measured with helium pycnometry (using a Multivolume Micromeritics AccuPyc II 1340, Norcross, GA USA) at room temperature. An eightfold determination was performed for the alginate sample. For the density of water a value of 997 kg/m³ (at 20 °C) was used.

In order to minimize the shrinkage and pore collapse typically observed in gel microstructures during drying, particularly in freeze- or ambient-dried samples, a well-established methodology for the supercritical drying of aerogels was applied [81]. These supercritically dried samples were subsequently used for Scanning Electron Microscopy (SEM) imaging (Zeiss Supra VP55, Jena, Germany) to investigate their inner pore structure. The preparation of the dried hydrogel samples includes a two-step procedure: First, water within the biopolymer structure was replaced by an organic solvent (usually ethanol) in a direct solvent exchange. Afterwards, the samples were sealed in filter paper bags and placed in an autoclave of 3.9 L volume. Supercritical CO_2 drying was performed at a pressure of 12 MPa and a temperature of 60 °C, with a continuous CO_2 flow (≈ 300 g/min) until complete extraction of ethanol was achieved (≈ 2 h drying time). Following depressurization, the aerogel samples were stored in sealed vessels inside a desiccator until SEM analysis. Prior to SEM imaging, the substrate was sputtered with a conductive, thin gold layer (≈ 6 nm, Sputter Coater SCD 050, BAL-TEC). The measurement was conducted under high vacuum using an Inlens detector (accelerating voltage = 3 kV, magnification = 100 000 x, and working distance = 5.6 mm). The SEM image was optimized regarding brightness and contrast with standard office tools (i.e., PowerPoint 2016).

Additionally, low temperature nitrogen physisorption was carried out to investigate the microstructural properties of the supercritically dried hydrogel samples (Nova 3000e Surface Area Analyzer, Quantachrome Instruments, Boynton Beach, USA). Before the measurement was conducted, the corresponding sample was degassed in a measurement cell under vacuum at 105 °C for ≈ 6 h. An amount of 20 mg to 30 mg was weighed for each run. The Brunauer–Emmett–Teller (BET) method was used to estimate the mass specific surface area (S_m) with a standard deviation based on a threefold determination.

Uniaxial compression tests of the original hydrogel particles were conducted using a texture analyzer (Stable Micro Systems Ltd., Surrey, United Kingdom) with a force resolution of ≈ 1 mN and a displacement resolution of ≈ 1 μm. The device recorded up to 500 data points per second. The measurement was started at a fixed position and the initial contact point was identified after the measurement via a postprocessing step to ensure precise identification. This was conducted using a Python script that calculated the running average of the recorded force data; the contact point of the measurement was defined as the moment when the running average showed a consistent increase, and all previous data points were excluded from further analysis. The stopping condition of all compression measurements was defined at a force of 100 N. The compression rate of the probe was varied within the range of 0.10 mm/s to 3.00 mm/s to assess its effect on the measured compression response and relaxation behavior of the biopolymer network, while the pre-compression speed was set to 0.20 mm/s in all experiments. Each test condition was replicated ten times, and the resulting force–displacement curves were used for analysis. Additionally, three video recordings were taken during each test condition to evaluate the apparent Poisson's ratio, transverse-to-axial ratio at 30% strain (TAR_{30}), and observe changes in the external shape of the particles. The initial point of the uniaxial compression measurements was used to determine the diameter of each hydrogel sample, which served as the basis for calculating strain and evaluating particle size distribution. In total 60 particles were analyzed. Circularity was determined through image analysis using ImageJ [67]. Five distinct images, each containing 10 hydrogel particles and a ruler for scale calibration, were analyzed.

2.1.3. Determination of the apparent Poisson's ratio and TAR_{30}

The apparent Poisson's ratio ν_{app} of the hydrogel sample is evaluated for the experimental compression test in the low-strain range up to 7.5% in accordance with Ed-Daoui and Snabre [24] and based on the linearization in Fig. A-2c in the Supplementary Material). In addition, the transverse-to-axial ratio at 30% strain (TAR_{30}) is analyzed for both the experimental and the simulated compression tests as a geometric descriptor of the compression behavior. To ensure better comparability between the two methods, the same optical analysis of particle shape under compression is applied, using a Python routine provided in the data availability link. Two different equations can be used to quantify the apparent Poisson's ratio. The first approach is based on comparing the volume change ΔV of the compressed hydrogel sample to the initial volume V_0. This leads to Eq. (2) using the change in height ΔL and the initial height L_0 of the hydrogel sample [30,51].

$$\frac{\Delta V}{V_0} = (1 - 2\nu_{\text{app}}) \frac{\Delta L}{L_0} \tag{2}$$

A second approach relies on the evaluation of the change of diameter ΔD and the initial diameter D_0 as stated in Eq. (3) [35].

$$\nu_{app} = \frac{\Delta d}{d}\frac{L}{\Delta L} \tag{3}$$

In addition, the TAR_{30} value was calculated using a mathematically equivalent expression to that used for the apparent Poisson's ratio in Eq. (3). The only difference is the applied strain range, which was extended to 30% strain to ensure comparability between simulation and experiment. The videos of the uniaxial compression test are used to evaluate the relative changes in the height L, diameter d and volume V during the compression. This was done in a semi-automated post-processing of the videos via Python. The manual steps included cropping the videos to center the hydrogel sample, and applying an Otsu filter [53] to the image, which resulted in a binary representation of the first frame. The baseline of the hydrogel sample is set manually, as an automatic determination of the baseline has shown challenges because of light reflection on the ground plate.

After the first frame has been modified, the following frames are processed in the same manner. In every frame, the Canny edge detection [11] is applied, which identifies the contour of the hydrogel sample. In the case of strongly deformed particles and light reflections, artificial contours might be identified. The correct contour representing the shape of the particle is identified with a reasoning pattern taking into account the baseline and the expected size and position of the contour.

The left and right halves of each hydrogel are evaluated independently. After some compression, spilled solvent accumulates in the region of the baseline, which results in an incorrect identification of the contour near the bottom of the sample. This is circumvented by clipping the contour above a certain threshold above the baseline. Additionally, the piston obscures the upper part of the hydrogel sample after a certain deformation. Therefore, the contour is clipped above the outermost points (in the horizontal direction), which represent the horizontal symmetry axis of the particle. The clipped contour thus represents only the lower half of the particle. In the subsequent analysis, symmetric deformation of the upper half of the particle was assumed as a geometric approximation to estimate particle height and diameter, following previous work [25,51]. Although this assumption may introduce some uncertainty at larger strains due to friction and geometric constraints, it provides a reasonable basis in the lower strain regime for the analysis. The diameter d is evaluated using the distance between the outermost points of both identified contours (in the horizontal direction). The height L is evaluated using twice the average height of the identified outermost points. The shape of the particle is described with a parabola, similar to the work of Nguyen et al. [51]. The parabola is fitted to the given points of the contour using the Least Squares Method. The parabola is constrained to pass through the outermost point, which corresponds to the diameter. The volume V is evaluated using the disc integration method applied to the parabolic function. An example of an unprocessed video frame from the experimental particle compression and the corresponding analysis of a single frame, showing baseline detection and the clipped contour of the particle's lower half, is presented in Fig. A-1.

Since the apparent Poisson's ratio and TAR_{30} characterize the relative change between the distances, an additional scaling to match absolute real-world dimensions is not required and thus all geometrical results from the video analysis are given in pixels.

2.1.4. Determination of the apparent Young's modulus

The raw force data were recorded without the application of a predefined trigger point, due to inherent noise and oscillations at the beginning of each compression measurement. To accurately identify the actual starting point of the compression, a Python routine was developed (Section C.2 of the Supplementary Material) that calculated the running average of the recorded force signal. Once the running average surpassed a defined threshold ("trigger value"), all previous data points were discarded (compare Fig. A-2a and b). This postprocessing step allowed for a more reliable and reproducible identification of the compression measurement start.

The resulting trimmed data set was then used to determine the apparent Young's modulus of each hydrogel particle. In contrast to cylindrical geometries, where the apparent Young's modulus can be obtained directly from the corresponding stress–strain curve, this approach is not suitable for spheres due to the difficulty in accurately measuring the time-resolved particle-probe contact area. Instead, the compressive response was determined based on the Hertz theory shown in Eq. (4).

$$F = \frac{4R^{0.5}}{3}\cdot\frac{Y_{app}}{1-\nu_{app}^2}\cdot\left(\frac{H}{2}\right)^{3/2} \tag{4}$$

$$Y_{app}^{*} = \frac{Y_{app}}{1-\nu_{app}^2} \tag{5}$$

This theory requires (i) the use of force–displacement data for which the Hertz model is valid and the value for the apparent Poisson's ratio ν_{app}, or (ii) alternatively only provides the reduced apparent Young's modulus Y_{app}^{*} defined in Eq. (5). The apparent Poisson's ratio was extracted from video recordings (see Section 2.1.3), whereas the valid initial range (usually up to about 5–10% strain) was identified following the linearization procedure proposed by Chan et al. [14] as illustrated in Fig. A-2c for 0.15 mm/s): After preprocessing of the raw force–distance data, the averaged displacement axis was transformed to $H^{3/2}$. A sequential expansion of the fitting region with least-squares regression was performed, and the optimal fitting interval was chosen from the regression diagnostics using the lowest Root Mean Squared Error (RMSE) as the selection criterion. Across all alginate hydrogels in this work this criterion led to an average valid region of 0.167 mm or 7.5% strain (compare [75]). An example of the linearization for a compression rate of 0.15 mm/s is given in Fig. A-2c. Subsequently, the Hertz theory in Eq. (4) was fitted to the experimentally measured force–displacement data within this range to determine the compressive apparent Young's modulus (illustrated in Fig. A-2d). Each compression rate was tested on ten independent hydrogel particles.

The apparent Young's modulus and apparent Poisson's ratio characterize the rate-dependent response of the coupled polymer matrix–fluid system and are therefore mainly used for comparative purposes.

2.2. Simulation

2.2.1. Setup and software

Our modeling approach focuses on representing the two distinct phases that make up a hydrogel: the alginate network and the aqueous phase. The alginate network is modeled using tetrapods, a polyhedral "parcel" composed of four distinct spheres, as introduced by Radl et al. [57]. This geometry is not intended as a molecularly-faithful representation of the alginate network topology, but rather as a phenomenological coarse-grained model calibrated to reproduce the macroscopic mechanical behavior of the hydrogel particle. This level of coarse-graining is a deliberate choice to enable scalability towards multi-particle simulations such as full particle beds, where microstructurally-resolved network representations would be computationally infeasible. Combined with a suitable force-model, it enables effective representation of the complex three-dimensional structure of a biopolymer network. The aqueous phase is represented by spherical water meso-particles that occupy the void space between the tetrapods.

The DEM simulation replicates the experimental uniaxial compression setup by employing a moving mesh wall that applies compressive forces to the hydrogel meso-particle. This simulation framework captures the mechanical response of the hydrogel under compression, including inter-particle interactions between tetrapods (i.e., the alginate network) and spheres (i.e., water). This enables us to generate the corresponding force–strain relationship for comparison and calibration with the respective experimental data.

All simulations in our present study are performed using a modified version of the LIGGGHTS® 3.8.0 [41] software tool.

Packing generation. The packing generation process involves the systematic placement of both particle types within a spherical domain and comprises the following steps:

- **Sphere placement:** Water meso-particles with a constant radius of 3.00×10^{-5} m are initially distributed within a spherical region of diameter 2.35×10^{-3} m using a face-centered cubic (fcc) packing. This setting for the water meso-particles represents a compromise between limiting computational cost and ensuring a sufficiently dense filling of the gaps between the tetrapods, so that no excessively large voids remain. The volumetric inflation of $19\,\%$ compared to the experimentally determined target hydrogel diameter d of 2.22×10^{-3} m is used to account for the cohesive interactions of the force model which leads to shrinkage in the subsequent equilibration. Thus, the final size of the simulated hydrogel particle can only be determined duing a postprocessing step because of this effect of the cohesive interactions.
- **Tetrapod placement:** Tetrapods are positioned using a two-stage approach. First, a shell of tetrapods (at the hydrogel particle's surface) is created using a Class I 4ν icosahedral geodesic sphere, resulting in 320 faces where each face defines the base area of one tetrapod [40]. Second, the remaining volume of the hydrogel particle is subdivided into 10 concentric shells, which are filled with randomly oriented and positioned tetrapods while maintaining constant volume fraction of tetrapods in each shell throughout each shell.
- **Size determination:** The radius of a tetrapod is determined based on the target alginate fraction w in the final hydrogel, which is set to 6.5 wt.%, resembling the experimental conditions as closely as possible. Consequently, the interlocking parameter ξ/D depends on the diameter of the target hydrogel d and the associated alginate fraction w, as shown in Table 1.
- **Overlap resolution:** After placement, any spheres that overlap with tetrapods are removed to prevent nonphysical configurations. This results in a hydrogel structure with the properties summarized in Table 1(a).

Precompaction and equilibration. To achieve a tighter packing within the hydrogel sphere, a precompaction step is applied after the initial packing generation. Following the approach developed by Clemmer et al. [16], a virtual spherical shell is implemented around the particle assembly. This boundary exerts repulsive forces on both tetrapods and spheres through a harmonic spring potential, effectively compressing the particle system inwards. In contrast to the original method by Clemmer et al., viscous damping is omitted from our implementation, as preliminary tests indicated that damping reduced the effectiveness of the compaction process. The precompaction procedure increases the initial particle volume fraction from $\approx\ 45\,\%$ to $\approx\ 50\,\%$, with the exact final packing density depending on the specific force parameters employed. After precompaction, the spherical shell is removed, leading to an equilibration within the final hydrogel-sphere. The resulting particle arrangement is illustrated in Fig. 1.

Uniaxial compression. To replicate the experimental compression protocol, the simulation procedure comprises the following sequential steps:

1. **Boundary setup:** Rigid walls are positioned at the maximum and minimum z-coordinates to establish compression boundaries for the hydrogel particle.
2. **Compression protocol:** The upper wall moves downward at a constant velocity v in the negative z-direction, applying uniaxial compressive loading to the hydrogel.

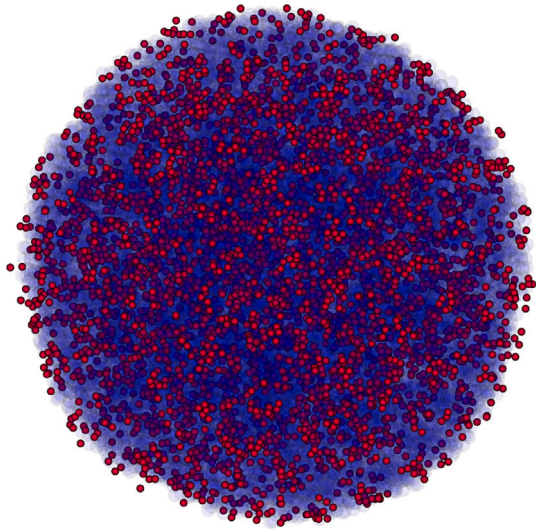

Fig. 1. Structure of a hydrogel sphere with (i) tetrapods (red) modeling the alginate network, and (ii) water meso-particles (blue) modeling the aqueous phase. (For interpretation of the references to colour in this figure legend, the reader is referred to the web version of this article.)

3. **Force measurement:** Contact forces are recorded exclusively on the upper wall during compression. These individual contact forces are subsequently integrated during post-processing to determine the total applied force.
4. **Strain reference definition:** The strain origin ($\epsilon = 0$) is established when the measured force F on the upper mesh wall first exceeds zero, ensuring accurate strain calculations from the initial contact point.
5. **Compression range:** The compression process is designed to capture the mechanical response up to $\epsilon = 0.50$. However, because the actual strain ϵ at each timestep is determined retrospectively during postprocessing, the simulation is extended to a nominal $\epsilon = 0.60$ to ensure that no relevant data is missed. This helps to eliminate the influence of the initial packing representing the hydrogel, which would lead to an overestimation of ϵ. Similar to the experimental setup, the starting point for our force–strain analysis is defined by the first timestep where a non-zero force on the upper mesh is observed.

2.2.2. Model details

The simulation utilizes the soft-sphere DEM approach to model particle dynamics and particle interactions (in what follows, particles refer to both tetrapods and water meso-particles). The fundamental governing equations are provided in Table A-2.

Force models. Our simulations employ a comprehensive set of force models incorporating multiple interaction mechanisms. The key components are structured as follows:

- **Contact forces:** Inter-particle contact forces are described by the classical Hertz-Mindlin contact model, which captures both normal and tangential force components during particle collisions. The corresponding mathematical formulations are detailed in Table A-3.
- **Rolling resistance:** Rolling torque effects are incorporated following the formulation by Iwashita and Oda [37], accounting for energy dissipation during particle rolling interactions.
- **Cohesive interactions:** Tetrapod-tetrapod and tetrapod-water interactions are modeled using a truncated harmonic potential defined in Eq. (6). This approach enables differentiated interaction strengths: stronger tetrapod-tetrapod bonds to represent the alginate network structure, and weaker tetrapod-water interactions to

Table 1
Simulation and packing generation parameters.

(a) Parameters used during packing generation. Subscript 1 = tetrapods, Subscript 2 = water meso-particles.

Parameter	Value	Unit
Mean hydrogel diameter d	2.22×10^{-3}	[m]
Tetrapod sphere diameter D	3.33×10^{-5}	[m]
Interlocking parameter ξ/D	4.10	[–]
Tetrapod density ρ_1	1723	[kg/m^3]
Number of tetrapods N_1	1196	[–]
Water meso-particle radius r_2	3.00×10^{-5}	[m]
Water meso-particle density ρ_2	997	[kg/m^3]
Number of spheres N_2	20,194	[–]

(b) Main simulation parameters.

Parameter (p = particle, w = wall)	Value	Unit
Young's modulus Y	1.0×10^8	[Pa]
Poisson's ratio ν	0.3	[–]
Coefficient of restitution e	0.3	[–]
Sliding friction coefficient $\mu_{\mathrm{rs}}^{[\mathrm{pp}]}$	0.7	[–]
Sliding friction coefficient $\mu_{\mathrm{rs}}^{[\mathrm{pw}]}$	0.4	[–]
Rolling friction coefficient $\mu_{\mathrm{rr}}^{[\mathrm{pp,pw}]}$	0.8	[–]

model water redistribution behavior. Inter-particle distances are calculated using normalized scaling factors and average particle radii as specified in Eq. (7). The model thus explicitly couples the solid network phase (tetrapods) with the interstitial fluid phase (water meso-particles). This is conceptually consistent with biphasic modeling frameworks, in which the mechanical interaction between a porous solid matrix and an interstitial fluid governs the rheological response of hydrated soft materials [26,50].

$$F_{\mathrm{ij}} = \begin{cases} 0, & \text{if } d_{ij} \le d_{\mathrm{eq,ij}} \text{ or } d_{ij} > d_{\mathrm{max,ij}} \\ 2h_{ij}\left(d_{\mathrm{eq,ij}} - d_{ij}\right), & \text{if } d_{\mathrm{eq,ij}} < d_{ij} \le d_{\mathrm{max,ij}} \end{cases} \tag{6}$$

$$\begin{aligned} d_{ij} &= r - (r_i + r_j) \\ d_{\mathrm{eq},ij} &= s_{\mathrm{eq},ij} \cdot \frac{r_i + r_j}{2} \\ d_{\mathrm{max},ij} &= s_{\max} \cdot (r_i + r_j) + \max_k r_k \end{aligned} \tag{7}$$

F_{ij} represents the cohesive force and h_{ij} denotes the interaction strength parameter. The surface-to-surface distance d_{ij} is determined from the center-to-center distance r and the particle radii r_i and r_j. The interaction range is governed by the equilibrium distance $d_{\mathrm{eq},ij}$ and the maximum cut-off distance $d_{\mathrm{max},ij}$, which are derived from the scaling factors $s_{\mathrm{eq},ij}$ and $s_{\max}$, respectively. Additionally, $\max_k r_k$ denotes the maximum particle radius within the simulation domain.

Model parameters: All associated force model parameters, including those for normal forces, tangential forces, and rolling torque, are typical values for tetrapods when used to model a network structure and are summarized in Table 1(b).

Calibration. The calibration of simulation parameters employs a systematic two-stage approach combining full-factorial design with advanced Bayesian optimization techniques. The methodology comprises the following sequential steps:

1. **Full-factorial design:** A complete factorial design with two levels (minimum/maximum) is applied to all 7 cohesion model parameters listed in Table 2, yielding $2^7 = 128$ parameter combinations. The parameter bounds are established through preliminary sensitivity analysis.
2. **Statistical significance analysis:** Significant parameters are identified by evaluating both main effects and two-parameter interactions using Analysis of Variance (ANOVA). Statistical significance is determined using a threshold of $p \le 0.05$.

Table 2
Parameters for full-factorial design with respective minimal and maximal values.

Parameter	Min	Max	Unit
h_{11}	10	1000	[N/m]
h_{22}	0.1	15	[N/m]
h_{12}	0	5	[N/m]
$s_{\mathrm{eq},11}$	1.93	2.00	[–]
$s_{\mathrm{eq},22}$	1.93	2.00	[–]
$s_{\mathrm{eq},12}$	1.93	2.00	[–]
$s_{\max}$	2.00	2.15	[–]

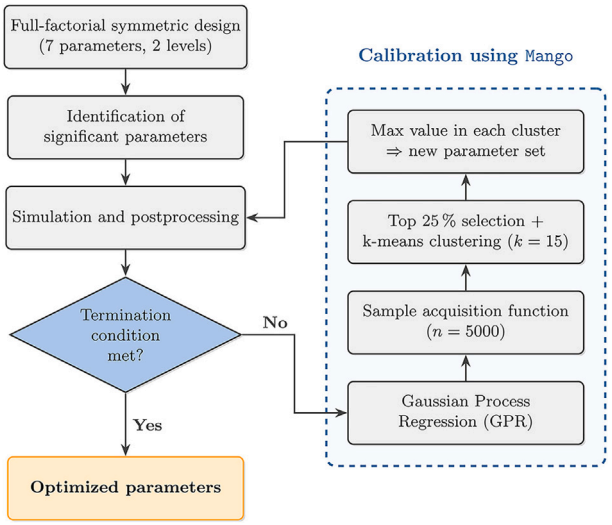

Fig. 2. Workflow diagram for parameter calibration using the Mango calibration framework [64,65]. The iterative process combines full-factorial design for initial parameter identification with advanced optimization techniques for Convergence to optimal parameter sets (adapted from Stadlthanner et al. [70]).

3. **Bayesian optimization:** Advanced parameter calibration is conducted using the Mango package [64,65] implemented in Python. The calibration framework employs the following specifications:
   - *Objective function:* Root Mean Squared Logarithmic Error (RMSLE) between simulation results and experimental force–strain data over the strain range $0.10 \le \epsilon \le 0.50$. Compared to the standard RMSE, the logarithmic transformation enhances sensitivity to small deviations in the force–strain curve, particularly at low strains and helps to fit the slope of the force–strain curve correctly.
   - *Surrogate model:* Gaussian Process Regression (GPR) to model the objective function response surface.
   - *Acquisition strategy:* Balanced exploration–exploitation approach with a batch size of 15 parameter sets per iteration.
4. **Convergence criteria:** To prevent unnecessary computational expense, the calibration terminates when both of the following conditions are satisfied:
   - Minimum of 5 iterations completed
   - Relative improvement $\Delta_t < 0.05$

   The relative improvement is calculated as stated in Eq. (8) where $f_{\mathrm{best}}^{(t)} = \min\{f(x_1), f(x_2), \ldots, f(x_t)\}$ represents the best objective value up to iteration t, and $\zeta = 10^{-8}$ prevents division by zero.

$$\Delta_t = \frac{f_{\mathrm{best}}^{(t)} - f_{\mathrm{best}}^{(t-3)}}{|f_{\mathrm{best}}^{(t-3)}| + \zeta} \tag{8}$$

Validation protocol: Following calibration, the best parameter set is validated through independent simulation runs using identical computational settings but with reduced compression velocities that match experimental conditions. This validation approach ensures model generalizability and prevents overfitting to the training data. The complete calibration workflow is illustrated in Fig. 2.

3. Results

3.1. Properties of alginate hydrogel particles

The physical characteristics and morphology of the investigated alginate based hydrogel particles are presented in Fig. 3. In order to gain insight into their microstructure, supercritical drying was performed to minimize shrinkage and pore collapse, thereby preserving the intrinsic pore structure. The resulting samples were characterized by nitrogen physisorption, revealing a specific surface area of $(350 \pm 16)\,m^2/g$ (determined by the BET method) and a mean pore diameter of (44.4 ± 2.0) nm. These measurements were performed in duplicate and fall within the typical range reported for alginate aerogels ($\approx$ 350 m^2/g to 600 m^2/g, compare [2,28,61]). The SEM image (Fig. 3(a)) further supports these findings, showing the characteristic porous morphology and confirming the presence of an open-pore network. Aerogels exhibit a predominantly mesoporous structure with additional macropores, as also evidenced by the SEM image.

The cumulative particle size distribution of 60 hydrogels (Fig. 3b) revealed that the bio-based particles have a relatively narrow size distribution within one batch, with an average diameter d_{50} of 2.22 mm. Nevertheless, it is known that the reproducibility of these bio-based gels is challenging due to aging and batch-to-batch variations [2]. Therefore, our present study focuses on a single hydrogel batch to specifically examine aging effects and avoid batch-to-batch variability. The investigated particles are highly spherical, with a sphericity Φ of 0.97. Due to the high water content ($\approx$ 93.5 wt.%), their density is close to that of water; for hydrogels prepared from a 2 wt.% alginate solution, this corresponds to a density of $\approx$ 1.026 g/cm^3.

The mechanical behavior of the hydrogels under uniaxial compression is visualized in Fig. 3(c). As the compression proceeds, the particles undergo progressive deformation, which is accompanied by a water distribution towards the outside ultimately visible as water release. This behavior is consistent with their highly hydrated internal structure and the elastic nature of the polymer network.

3.2. Apparent rate-dependent compression behavior

The qualitative deformation behavior shown in Fig. 3(c) indicates that the mechanical response of hydrogels under load is coupled with water drainage from the polymer network. Given the hydrated and porous nature of the investigated material, the compression response reflects both network deformation and fluid flow. Accordingly, the parameters derived from compression tests are considered as apparent quantities governed by the applied compression rate. To quantitatively assess the apparent rate dependence, the uniaxial compression data were analyzed using force–strain instead of force–distance plots to minimize artifacts associated with the inherent size polydispersity of hydrogel particles (compare Fig. 3b). The resulting profiles in Fig. 4(a) exhibit a pronounced rate-dependent response, reflected in the systematic dependence of the loading behavior on the applied deformation rate from 0.10 mm/s to 3.00 mm/s (6 mm/min to 180 mm/min). The magnified view highlights that increasing compression rate results in progressively steeper force–strain curves, indicating enhanced resistance to deformation at higher loading rates. This effect is presumably attributed to coupled viscoelastic and fluid-transport effects, including restricted relaxation dynamics and reduced water mobility within the hydrogel matrix under rapid compression [24,55,75]. However, a limitation of the compression measurement is that it alone does not separate intrinsic network elasticity from poroelastic and viscoelastic contributions. To identify the pure material network constants, either independent compression experiments with for instance aerogels or a constitutive model would be required that explicitly separates fluid and network stresses.

Nevertheless, no indications of structural failure in terms of breakage are apparent at the tested compression rate range until 3.00 mm/s

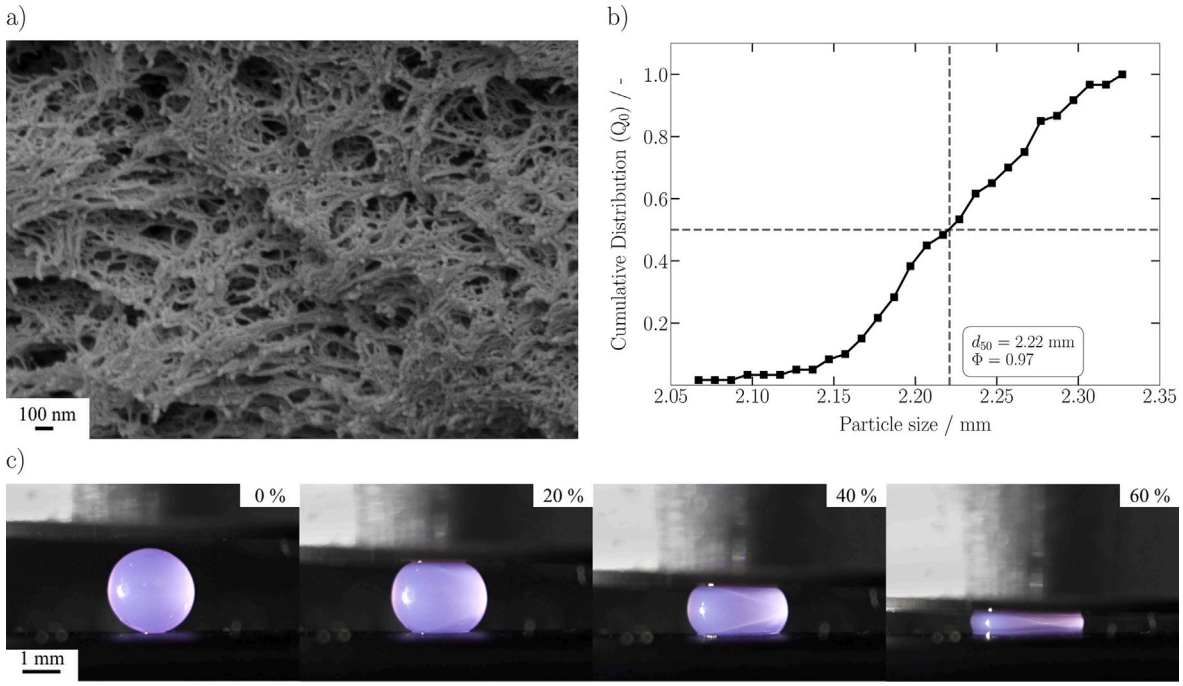

Fig. 3. Characterization of the investigated 2 wt.% alginate hydrogel particles: a) scanning electron microscopy (SEM) image with a magnification of 10^5 after solvent exchange and sc. drying of the hydrogel sample, b) particle size distribution of 60 hydrogel particles including the mean particle diameter d_{50} and sphericity Φ c) hydrogel particles under uniaxial compression with the observed strains given in percentage at a compression rate of 0.30 mm/s.

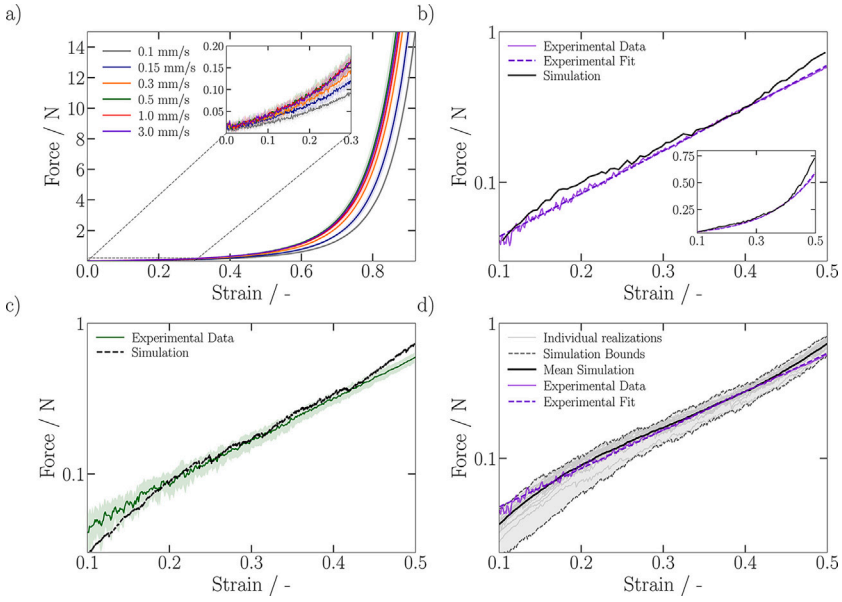

Fig. 4. Force–strain data from uniaxial compression: a) loading experiments showing the effect of probe velocity ranging from 0.10 mm/s to 3.00 mm/s, b) simulation data at a uniaxial compression rate of 3.00 mm/s with optimized parameter-set (see Table 3(a))) (red) and experimental data (black), both raw (solid) and fitted (dashed) with RMSLE = 0.1201; c) validation of tetrapod simulation data with experimental data at a compression rate of 0.50 mm/s (data for 0.30 and 1.00 mm/s are presented in Figs. A-9 and A-8 in the Supplementary Material; d) force–strain response of the tetrapod simulations at 3.00 mm/s showing mean behavior (solid line) with uncertainty bands (shaded area) representing the envelope of the data (min - max) from 20 packing realizations. Individual realizations are shown as thin gray lines. (For interpretation of the references to colour in this figure legend, the reader is referred to the web version of this article.)

(visible for single loading experiments until strains of ≈ 50% in Fig. A-3). Previous studies have reported that, above ≈ 0.60 mm/s, the mechanical response remains virtually unchanged with respect to further increases in compression rate [73]. In agreement with this, the data reveal a comparable transition, with the onset of apparent rate-independent behavior emerging around 0.50 mm/s.

3.3. Sensitivity analysis and calibration of the tetrapod simulations

Using the approach outlined in Section 2.2.1, the simulations aim to reproduce the experimentally observed force–strain behavior and thereby provide insight into the internal force distribution within a hydrogel particle. For a quantitative comparison between experimental and simulated force–strain curves an objective function is needed which is defined as the RMSLE between experimental and simulation results for $0.10 \leq \epsilon \leq 0.50$, as outlined in Section 2.2.2. However, this requires fitting the experimental data first. Using an exponential fit of the form $F(\epsilon) = a \cdot \exp(b \cdot \epsilon)$, a coefficient of determination of 0.9978 was achieved. The fitted equation used for all further considerations is shown in Eq. (9).

$$F(\epsilon) = 0.023 \cdot \exp(6.551 \cdot \epsilon) \tag{9}$$

The parameter calibration is conducted for the highest compression rate (3.00 mm/s) to minimize computational effort during calibration. The simulation success rate during the initial full-factorial design is 79.7 %, indicating certain limitations in the model at the chosen minimal and maximal values as stated in Table 2. Nevertheless, five parameters were identified as significant, having p-values ≤ 0.05 either as singular effects or within two-parameter interactions. All significant effects, as well as thresholds of significance and the first non-significant effect are shown in Fig. A-7. The most influential parameters are the maximum neighbor distance d_{max} and the harmonic stiffness between tetrapods h_{11}. For the two non-significant parameters, $s_{eq,22}$ and $s_{eq,12}$, the mean of minimal and maximal values covered in the full-factorial design, in both cases 1.965, was used.

Following the full-factorial design, a batch Bayesian optimization was performed to find the optimal parameters for the simulation. The calibration process was run for 8 iterations with batches of 15 simulations each. The simulation results using the optimal parameter set (summarized in Table 3(a)) are shown in Fig. 4(b). The optimized values indicate that the interaction between tetrapods (governed by h_{11} and $s_{eq,11}$) is responsible for the major part of the force–strain response. Furthermore, the interaction between tetrapods and water mesoparticles (associated values h_{12} and $s_{eq,12}$) is low, as was desired to allow for movement of the spheres within the tetrapod network. The calibration process converged to a set of parameters that minimized the RMSLE between the simulation data and the fitted experimental data following the convergence criteria defined in Section 2.2.2. A total of 248 simulations were performed during this process, 128 of which were in the full-factorial design, with the rest conducted during subsequent calibration steps. The optimized result was identified after 5 iterations, as shown in

Table 3
Optimized model parameters and validation results for different uniaxial compression rates.

(a) Optimized parameters for a uniaxial compression rate of $v = 0.00$ m/s.

Parameter	Value	Unit
h_{11}	233	N/m
h_{22}	5.12	N/m
h_{12}	1.98	N/m
$s_{eq,11}$	1.98	–
$s_{eq,22}$	1.97	–
$s_{eq,12}$	1.97	–
s_{max}	2.10	–

(b) Validation results, expressed as RMSLE values, for lower uniaxial compression rates v.

Rate v mm/s	RMSLE
0.3	0.1725
0.5	0.0332
1.0	0.1179

Table A-6. To satisfy the convergence criteria defined in Section 2.2.2, 3 additional iterations were performed, yielding no improvement in RMSLE.

3.4. Validation

After the parameter calibration was performed at a relatively high compaction rate of 3.00 mm/s to minimize computational effort, the resulting parameter set was validated using simulations at lower compression velocities. The corresponding results and deviations from the experimental data for the strain interval between 0.1 and 0.5 are summarized in Table 3(b). Additionally, the logarithmic-scale force–strain profile of the experimental data and the simulation for a compression rate of 0.50 mm/s is presented in Fig. 4(c), showing a high degree of agreement, particularly within the strain range of 0.2–0.4. Further validation data at 0.30 mm/s and 1.00 mm/s are provided in Figs. A-9 and A-8 in the Supplementary Material. Overall, an RMSLE $\leq$ 0.18 applies for all investigated uniaxial compression velocities, with the highest error being observed for the lowest rate used in validation. These results confirm that the optimized parameter set remains valid across the entire range of relevant compaction velocities. Further considerations as well as additional validation simulations are outlined in Section D.2 of the Supplementary Material.

3.5. Uncertainty quantification

Experimental data inherently exhibit a certain degree of variability due to (i) environmental influences during testing, as well as (ii) initial inhomogeneities in the polymer network introduced during the sample preparation, particularly during the gelation process, even when the same particle batch is used for all experiments (compare Section 2.1.1, see [60]). In this context, recent hydrogel simulation studies [77] have shown that network heterogeneity can strongly influence the mechanical response, highlighting the importance of structurally informed phenomenological modeling for hydrogel mechanics. In the simulations, variability instead originates from the randomized placement of tetrapods during packing generation. This random process of insertion into shells during packing generation, detailed in Section 2.2.1, significantly influences the mechanical response of the hydrogel model.

Therefore, twenty different packing configurations were generated using different random seeds. All other parameters remained constant at their optimized values in Table 3(a). This ensemble was used to characterize packing-induced variability under otherwise identical simulation conditions. Stochastic insertion affects several critical aspects of the final microstructure. Notably, the overlap resolution procedure yields different water meso-particle counts in each realization. Specifically, we observed $\overline{N_S} = 20\,231$ meso-particles with a standard deviation of $s_{N_S} = 61$. This structural variation directly impacts the mechanical response. Table 4 presents the statistical distribution of key micro-structural parameters and corresponding force values at selected strain levels. Packing-induced variability changes with strain and decreases with deformation. To quantify this, the coefficient of variation CV as defined in Eq. (10) is used.

$$\mathrm{CV} = \frac{s}{\bar{x}} \tag{10}$$

The coefficient of variation decreases from 1.25×10^{-1} at $\epsilon = 0.20$ to 8.15×10^{-2} at $\varepsilon = 0.5$. This trend aligns well with the experimental observations, where the coefficient of variation drops from 1.41×10^{-1} to 6.34×10^{-2} over the same strain range. Fig. 4(d) illustrates this trend for a compression rate of 3.00 mm/s through the mean response and associated data envelope spanning the associated minimal and maximal values of all 20 samples. This indicates, that micro-structural differences present in the beginning vanish or become insignificant at higher strains. Consequently, the impact of the initial arrangement is reduced and the strain response is uniquely determined by the parameter set.

Table 4
Statistical analysis of uncertainty due to packing generation and the resulting force–strain response (20 realizations) including the mean $\bar{x}$, the standard deviation s, the coefficient of variation CV, and the coefficient of variation of the experimental data $\mathrm{CV}_{\mathrm{exp.}}$.

Parameter	$\bar{x}$	s	CV	$\mathrm{CV}_{\mathrm{exp.}}$	Units
Number of spheres N_S	20,231	61	3.00×10^{-3}		[–]
Alginate fraction w	6.54	0.02	2.80×10^{-3}		[wt.%]
Force at $\epsilon = 0.20$	0.09	0.011053001	1.25×10^{-1}	1.41×10^{-1}	[N]
Force at $\epsilon = 0.40$	0.31	0.02593252	8.34×10^{-2}	7.03×10^{-2}	[N]
Force at $\epsilon = 0.50$	0.71	0.057591779	8.15×10^{-2}	6.34×10^{-2}	[N]

Deterministic, ordered packing arrangements could theoretically further reduce this variability. However, such configurations would introduce artificial symmetries and unrealistic force transmission patterns [7,82]. These artifacts do not represent the natural disorder characteristic of real hydrogel micro-structures. Therefore, the tetrapod model should be understood as a phenomenological representation of the real hydrogel particles. Experimentally, hydrogel samples exhibit inherent structural heterogeneity due to biopolymer synthesis and gelation processes, even when produced within a single batch (see Section 2.1.1). While in the simulations, variability arises from differences in the random packing configurations generated for the tetrapod-based hydrogel model. The packing-induced simulation variability shows a qualitatively similar strain dependence to the experimental scatter, as shown in Fig. A-3. This suggests that the model captures an important aspect of the microstructural variability relevant to the mechanical response. However, the similarity in the coefficient of variation should not be interpreted as evidence that the physical origins of variability are identical in both cases.

3.6. Aging and shape function

While our representation of the (randomized) tetrapod packings successfully accounts for microstructural heterogeneity and its impact on mechanical variability, it does not capture time-dependent alterations in material properties arising from storage-related effects. In biopolymer-based hydrogels, such aging-related processes constitute an additional source of variability, alongside challenges in batch-to-batch reproducibility caused by environmental influences, intrinsic variability of biopolymers, and the gelation process itself. As a result, direct comparison of mechanical properties is complicated, as they are strongly affected by both fabrication and storage. Consequently, the present study does not address batch-to-batch variations but instead focuses on hydrogels from a single batch to specifically examine aging effects.

Aging of the biopolymer-based hydrogels over the course of approximately one year resulted in a pronounced stiffening of the material especially for $\epsilon \geq 0.10$ as well as a slight increase in the mean particle size to 2.44 mm while the circularity of the particles stayed nearly constant (see Figs. 5(a) and A-4). The force–strain curves show a systematic increase in the required force at comparable strain levels from day 1 to day 351, indicating a continuous densification or reinforcement of the internal network. This observation contrasts with existing literature, where hydrogel aging is often associated either with a weakening of the network due to the progressive loss of Ca^{2+} crosslinking or with a rapid stiffening that typically reaches equilibrium within the first two weeks [4,15,42]. A comparable time-dependent evolution of poroelastic properties has been reported for agar hydrogels during ambient drying, where progressive water loss stiffens the network [23]. Nevertheless, to the best of the authors' knowledge, no long-term studies extending beyond this period are available. In the present study, no such plateau was observed; instead, the mechanical response continued to evolve over several months.

One could argue that the addition of sodium azide, used to prevent microbiological degradation of the hydrogel particles, may have

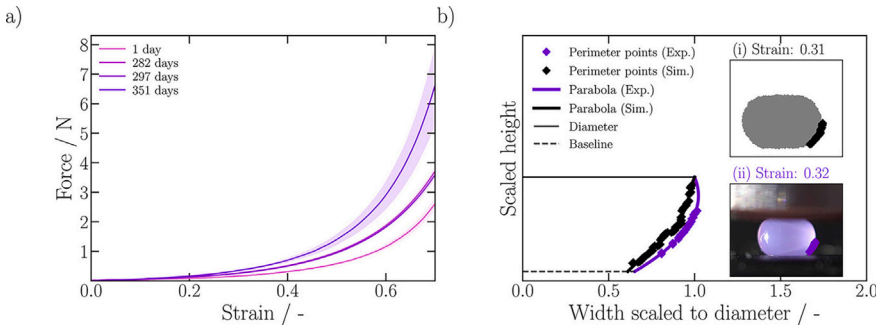

Fig. 5. a) Influence of aging on the mechanical behavior of biopolymer-based hydrogels over a period of approximately one year. All experimental results are presented as mean values (N = 10 samples); hatched areas indicate the standard deviation. b) Experimental and simulated hydrogel particle morphologies at $\epsilon = 0.3$ including insets of the corresponding particle frame used for the analysis: i) tetrapod simulation and ii) real hydrogel.

influenced the results. However, this additive solely inhibits microbial growth and does not interfere with Ca^{2+}-ion exchange, and therefore does not affect the intrinsic aging of the polymer network. To ensure comparability between the initial and aged uniaxial compression experiments, an age-dependent correction factor was applied to account for changes in mechanical response induced by the aging process. The correction was performed in such a way that the mechanical response of the unaged samples served as the standardized reference for all subsequent measurements.

In addition to the quantitative comparison of the simulation results with the experimental uniaxial compression data, the visual deformation behavior of the hydrogel particles was evaluated. This method is in line with the analysis approach described by Nguyen et al. [51], where they manually identified the boundary points of the side-view projection, which were subsequently fitted using a parabolic curve to describe one quadrant of the contour. In our present work, the outer particle contour was extracted using a Python-based image analysis workflow, in which the right quadrant of the side-view projection was analyzed (methodological details are provided in Section 2.1.3). The results of this visual assessment are shown in Fig. 5(b). Due to the smooth surface of the hydrogels, an exact determination of the particle contour in the experimental images is challenging, resulting in fewer boundary points that can be used for fitting the contour function. In contrast, the simulated particles have a rugged contour, as they are composed of primary particles and tetrapods rather than a continuous surface, which facilitates more precise extraction of the outer contour. Nevertheless, both the experimental and simulated outer shapes followed similar scaling trends when normalized to particle diameter. These results demonstrate that the simulation is not only able to describe the mechanical response accurately but it also captures the macroscopic deformation behavior of the hydrogel particles at a strain of 30%.

3.7. Cyclic loading

Having established that the simulated particle geometry reproduces the experimentally observed macroscopic contour deformation at 30% strain, the analysis now extends to the mechanical response during cyclic loading. Specifically, the behavior of hydrogel particles at different strain levels under such loadings is evaluated first. In the elastic regime (i.e., $\epsilon \leq 0.2$), the experimental loading–unloading curves show a consistent, non-linear force–strain response with low hysteresis (see Fig. 6(a)). Individual measurements across ten distinct particles show only minor variability, while the averaged curve of these samples highlights the reproducible nature of the deformation behavior.

Across all cyclic tests conducted at a compression rate of 3.00 mm/s, an initial increase in force is observed at the beginning of the loading stage, which levels off at $\epsilon \approx 0.06$ (compare Fig. A-5). This effect is attributed to the low pre-compression rate used before switching to the target test rate. To ensure consistency across all experiments, the pre-compression rate was kept constant for all tests, which makes this transient effect particularly pronounced at high compression velocities. In contrast, at 0.30 mm/s, this behavior is not observed, as the difference between pre-compression and test rate is relatively small (see Fig. A-6). Further cyclic measurements in the strain range of 20–60% at both velocities (0.30 and 3.00 mm/s) are provided as individual measurements (see Fig. A-5 and A-6). These results confirm that the elastic regime of the hydrogels under uniaxial compression extends to at least $\epsilon = 0.30$ and is independent of the applied compression rate.

In addition to the force–strain curves, the particles were examined before and immediately after compression using the open source software ImageJ to quantify irreversible changes in particle height (example images for $\epsilon = 0.60$ are given in Fig. 6(c)) [67]. These measurements revealed that, for both compression velocities (0.30 and 3.00 mm/s), visible plastic deformation exceeding 30 % occurs only when the particles are loaded beyond $\epsilon = 0.50$ (see Table A-5).

At these higher deformation levels (60% strain), the experiments reveal pronounced non-linearity and plastic deformation (Fig. 6(c)). After unloading, the particles do not fully recover to their original shape, as illustrated by the inset images in Fig. 6(c), which show a height reduction of ≈ 12.6 %. The force increases steeply at large strains, and the hysteresis loop widens compared to the 20% strain cyclic loading experiments, reflecting irreversible structural rearrangements within the hydrogel. The averaged curve again confirms the reproducibility across ten independent measurements.

These findings are consistent with the elastic limit reported by Wang et al. [75], who demonstrated full recovery of alginate hydrogel particles up to $\epsilon = 0.50$ and consequently selected $\epsilon = 0.30$ deformation as a standard testing strain to ensure elastic behavior. This observation is further supported by the results of Chan et al. [14], who identified plastic deformation at $\epsilon \geq 0.5$. Thus a similar approach is adopted in the present work to determine material parameters within the elastic deformation regime, where $\epsilon = 0.30$ corresponds to a particle height reduction of ≈ 0.66 mm.

While the calibration and initial validation of the tetrapod simulations were performed using only monotonic uniaxial compression, the agreement between experimental and simulation results for cyclic loading behavior was also investigated to test the ability of the model to capture hysteretic responses. The loading cycles were performed by applying uniaxial compression to a set strain level ϵ, followed by immediate decompression in the positive z-direction at the same rate (3.00 mm/s) to avoid apparent rate-dependent effects.

Our analysis of the experimental data (see Fig. 6(a)) indicates a mainly elastic behavior with complete strain recovery at lower strains ($\epsilon \leq 0.20$), transitioning to irreversible plastic deformation at higher strains ($\epsilon \approx 0.60$). Although data from individual simulation runs exhibit stochastic variations (due to the random nature of the tetrapod packing), our averaged simulation data align well with the experimentally

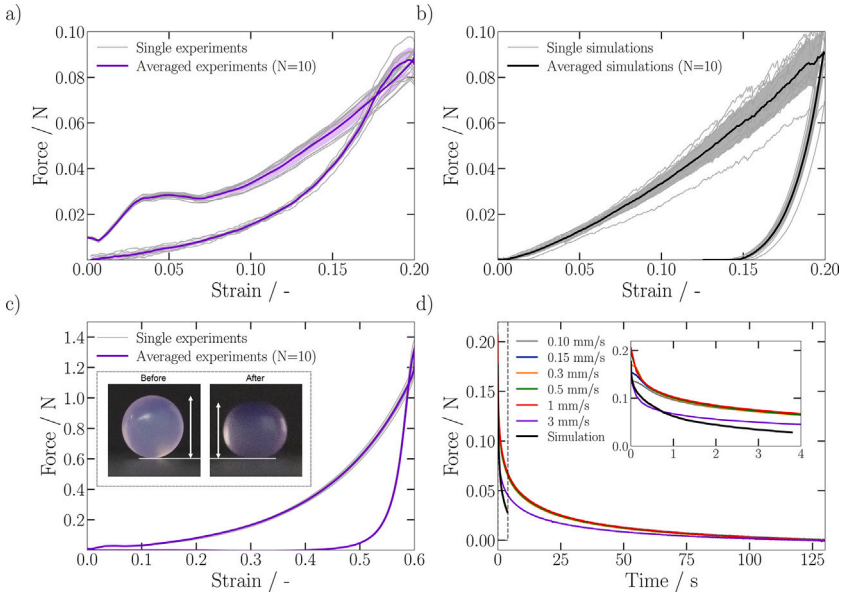

Fig. 6. Loading–unloading behavior of hydrogels at 3.00 mm/s: a) experimental data within the elastic regime ($\epsilon = 0.20$), b) tetrapod simulation ($\epsilon = 0.20$) and c) plastic deformation beyond the elastic limit ($\epsilon = 0.60$). d) Force–relaxation response after loading to $\epsilon = 0.30$ at various compression velocities (0.10 mm/s to 3.00 mm/s); inset compares experimental and simulated relaxation at 3.00 mm/s (first 3.7 s). Experimental relaxation lasted 130 s. All experiments/simulations are shown as averaged data (with N = 10 samples); hatched areas represent the standard deviation. Gray thin lines in a)–c) describe the single particle experiments/simulations.

observed loading branch of the force curve (compare Fig. 6(a) and (b)). Our simulations, however, show plastic deformation already at much lower strain levels (i.e., $\epsilon \approx 0.20$, see Fig. 6b), indicating increased energy dissipation and stronger damping compared to the experimental results for which this is observed at significantly larger strains (i.e., $\epsilon \approx 0.60$, see Fig. 6(c)). This discrepancy suggests that our current model overpredicts irreversible structural changes in the hydrogel at small strains, and hence energy dissipation during cyclic loading.

3.8. Relaxation

To further characterize the viscoelastic damping behavior and validate the capability of the model to reproduce time-dependent material responses, stress relaxation simulations were performed following the same protocol as the corresponding experiments: After the samples were compressed to 30% strain, staying within the elastic regime, the displacement was held constant and the decreasing reaction force on the compression plate was continuously recorded. The corresponding results are shown in Fig. 6(d).

Across the tested compression rates (0.10 mm/s – 3.00 mm/s), the force decreases rapidly during the first few seconds, followed by a slower, asymptotic relaxation over the remaining holding period. As expected from previous results, higher compression velocities produce larger initial peak forces. Existing studies indicate that an increase in compression rate facilitates a more rapid decrease in force during the subsequent relaxation phase [75]. However, in the present analysis, a clear rate-dependent trend emerges exclusively at the highest applied compression rate. In contrast, the relaxation responses recorded at lower velocities (0.10 to 1.0 mm/s) exhibit minimal to no rate-induced differences.

The insert in Fig. 6(d) compares the experimental relaxation response at 3.00 mm/s with the corresponding tetrapod simulation. In contrast to the experiments, the simulation was only performed at this compression rate due to the enormous computational effort that would be required at smaller rates. The simulation yields a total holding time of 3.7 s, throughout which the imposed deformation is kept constant to capture the material's transient force response.

Similar to the loading-unloading behavior, the relaxation simulations show, despite the significantly shorter relaxation time, there is significantly faster energy dissipation compared to the experimental results. This consistent discrepancy across different test conditions suggests a fundamental limitation in our current model formulation. This is probably related to the damping mechanisms or time-dependent material properties. However, it is important to note that the model calibration was based on monotonic uniaxial compression (i.e., "loading") data only, and despite the quantitative differences, the qualitative behavior between simulation and experiment remains similar. This indicates that the model captures the general trends of the material response. Further efforts to calibrate the models' viscoelastic damping behavior were forgone due to limits in computational resources. Considering the fact that our cohesive interactions were modeled with a harmonic potential (see Eq. (6) and (7); i.e., a fully elastic model), it suggests that a more substantial analysis of our force models is needed to improve our predictions for cyclic loading.

3.9. Elastic behavior: apparent Young's modulus and transverse-to-axial ratio at 30% strain (TAR_{30})

Building on the uniaxial compression behavior investigated in Fig. 4, the elastic response and the apparent effect of deformation rate were systematically evaluated. This enables a more detailed comparison between experiments and tetrapod simulations using the apparent Young's modulus and the TAR_{30} value, while also providing insight into the time-dependent coupled mechanical response of the biopolymer network and water drainage.

Fig. 7(a) presents the TAR_{30} value as a function of longitudinal strain at a piston velocity of 3.00 mm/s, together with the apparent experimental Poisson's ratio at a strain of 7.5%. The investigated strain range corresponds to a small to moderate deformation, in which the hydrogel response departs from elasticity while remaining free of macroscopic instabilities. In this regime, microstructural reorganization, water flow and poroelastic effects become increasingly relevant.

The experimental data are presented as triplicates with the standard deviation indicated by shaded areas. Within the investigated strain range and at the applied compression rate, the TAR_{30} increases continuously with strain, thereby indicating a gradual transition toward quasi-incompressible behavior (i.e., a restriction of volumetric deformation is observed). This behavior is presumably caused by network

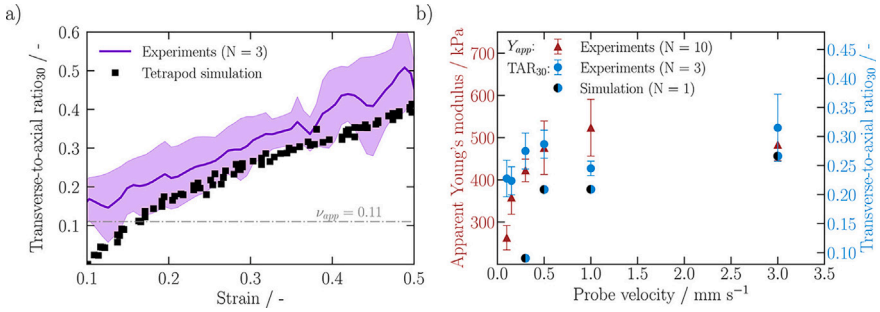

Fig. 7. Experimental data of hydrogel response and predictions with our tetrapod model (piston velocity of 3.00 mm/s): a) TAR_{30} versus strain, together with the apparent Poisson's ratio at 7.5% strain. The experiments were performed as triplicates with the hatched area representing the standard deviation. b) Impact of deformation rate on apparent Young's modulus and TAR_{30}. Data points shown correspond to averages (based on N repetitions), and error bars represent the standard deviation.

densification, pore closure, and restricted fluid mobility. The tetrapod simulations qualitatively reproduce this experimental trend; however, the simulated values are systematically lower than our experimental measurements, particularly at lower strains. This suggests that while the underlying mechanical densification mechanism of the polymer network is captured by our model, the higher values observed in our experiments likely reflect additional poroelastic effects in our hydrogel particles.

In contrast, the apparent Poisson's ratio, determined for strains up to 7.5%, exhibited no dependence on compression rate and was therefore averaged across all samples, yielding a value of 0.103 ± 0.031. This value was subsequently used to calculate the apparent Young's modulus. However, it is notably lower than literature values, for instance, Nguyen et al. reported typical values of approximately 0.3 [51]. The lower values observed in the present study may be attributable to drainage or poroelastic effects during the experiment, where water is redistributed within the bead or expelled from it. Additionally, a strong strain dependence is evident, as reflected by the progressive increase in the TAR_{30} value, which further supports this assumption.

The influence of compression rate on the apparent elastic properties of the hydrogels is further examined in Fig. 7(b). Both apparent Young's modulus and TAR_{30} are plotted as functions of compression rate ranging from 0.10 to 3.00 mm/s. While the apparent Young's moduli were determined as mean values from ten particle compression measurements, the TAR_{30} was calculated based on three video recordings of our compression experiments. With increasing compression rate, both parameters initially exhibit a pronounced increase. Beyond a threshold deformation rate (i.e., ≈ 0.50 mm/s), the apparent Young's modulus and TAR_{30} approach a plateau, indicating a saturation regime in which further increases in rate have only a minor effect on the coupled response. This behavior is consistent with previous observations for hydrogels subjected to dynamic loading (compare Section 3.2). This apparent rate-dependent response can be attributed to the limited time available for network relaxation and fluid redistribution under faster deformation. At low probe velocities, the biopolymer network has sufficient time to adapt to the applied stress, resulting in lower apparent stiffness and reduced resistance to volume changes. Such behavior has been widely reported for biopolymer and hydrogel systems in both theoretical and experimental studies [24,55].

In general, the experimentally determined reduced apparent Young's moduli (see Table A-4, calculated based on Eq. (5)) cover a slightly greater range than those reported by Wang et al. [75]. While their measurements range from ≈ 220 to 450 kPa, depending on the compression rate, the reduced apparent moduli obtained in our present work range from 190 to 562 kPa. These values are consistent with other previously reported apparent rate-dependent strain-stiffening behavior of the coupled matrix-fluid system. Comparable ranges of apparent Young's moduli have further been reported for sodium alginate hydrogels cross-linked with $CaCl_2$ by [14,73].

A similar rate-dependent trend is observed for the TAR_{30}, which increases with compression rate and approaches values close to 0.3 (see Fig. 7b). At a compression rate of 0.50 mm/s, a TAR_{30} value of 0.29 is obtained. Only our result at a compression rate of 1.00 mm/s deviates unexpectedly (i.e., too low values) from this trend, despite being measured in triplicate. The observed saturation of the TAR_{30} at higher velocities points to a rate-independent mechanical regime, in which further network rearrangement and fluid redistribution are constrained.

Overall, the tetrapod simulations qualitatively reproduce the experimentally observed trends of the TAR_{30}, capturing both the initial stiffening at low compression rates and the subsequent saturation behavior. Due to the computational constraints of the simulations, only one simulation run per compression rate was performed, resulting in a residual uncertainty in our simulations. Nevertheless, the simulations slightly underestimate the lateral strain response, suggesting that additional mechanisms contributing to transverse deformation may not yet be fully captured by our model.

3.10. Performance considerations

Using the parameters stated in Table 1(b) on a single node of a high-performance computing (HPC) cluster equipped with Intel® Xeon® E5-2640 v4 (10 cores, 20 threads, 2.40 GHz) results in a wall time of about 2.5 days for a typical simulation, depending on the specific parameters. With the time step chosen based on 10 % of the Rayleigh time step, one could simply decrease Y to decrease the wall time ($t \propto \sqrt{Y}$) [71]. Thus, within the limit of $Y \geq 5.00 \times 10^6$ J/m^3 in LIGGGHTS® 3.8.0, t can be increased by a factor of ≈ 4.5. Simulations using reduced apparent Young's moduli were performed and are shown in Fig. A-10. The actual factor of improvement in wall time by reducing Young's modulus to its lowest possible value was ≈ 3.9 due to the longer wall time per time step. Clearly, additional calibration would be required to match the experimental data using the adapted setup, which was omitted in our present study, as a qualitative match was already established using the parameters from Table 3(a).

3.11. Alternative model using spheres to represent the alginate network

Several alternative model configurations were explored to assess the sensitivity of our predictions. For example, the implementation of flexible tetrapods, as presented by Radl [56], was investigated but did not yield improved performance. Furthermore, the geometric sensitivity was analyzed by replacing tetrapods with an equal amount of "structural spheres" (i.e., spheres connected with cohesive forces), maintaining a constant weight fraction. However, this configuration resulted in fundamentally different force–strain behavior, with force transmission occurring primarily through water meso-particles rather than the substituted structural spheres, as shown in Fig. A-12. The force

distribution in the gel at $\epsilon = 0.6$ using tetrapods is shown in Fig. A-11: panel a) shows the probability distribution of contact forces, and panel b) shows the tetrapod contact-force network. Clearly, the majority of the force is distributed through the tetrapods, similar to the force distribution through the alginate network in the actual hydrogel. These findings emphasize that the tetrapod geometry is crucial for the accurate representation of the hydrogel microstructure and force transmission networks.

4. Conclusion and outlook

In our present study, the apparent rate-dependent mechanical behavior of alginate-based hydrogel particles under uniaxial compression was investigated through both experimental characterization and a novel tetrapod-based Discrete Element Method (DEM) framework. The experiments revealed a pronounced apparent rate-dependent response and strain-stiffening behavior, reflected in an increasing resistance to deformation with increasing compression rate. Above a critical probe velocity of $\approx$ 0.50 mm/s the mechanical response became largely rate-independent, indicating a saturation regime in which network relaxation and fluid redistribution are increasingly constrained. Comparable trends were observed in the apparent elastic regime, affecting both the TAR_{30} value and the apparent Young's modulus. Cyclic loading experiments further confirmed that the hydrogels behave elastically up to $\epsilon \approx 0.5$, while higher strains induce plastic deformation. This experimental data set provides input parameters for the simulation approach and supports the calibration and validation, thereby enabling physically grounded modeling. In addition, long-term aging experiments demonstrated a continuous stiffening of the hydrogel network over several months, showing storage effects in biopolymer-based systems.

The proposed tetrapod-based simulation framework employs a rarely explored biphasic DEM simulation approach. It represents hydrogels as distinct solid (polymer network) and liquid (water) phases, set up using experimental data such as water content in real hydrogel spheres. The experimentally observed force–strain behavior was successfully reproduced across a wide range of compression rates, using a calibrated parameter set. The model was validated with a separate data set (unseen during calibration), demonstrating good transferability and confirming that the calibrated parameters are not restricted to a specific loading condition. This approach identifies the alginate network as the primary load-transmitting phase while allowing the embedded water to flow within this structure. It mimics the real hydrogel structure and depicts force distribution across the polymer network under compression, information usually inaccessible via experiments. Moreover, our stochastic generation of the tetrapod packings introduces a level of variability that closely resembles the experimentally observed scatter, thereby enhancing the physical representativeness of the model. Beyond the quantitative description of mechanical behavior and stochastic variability, macroscopic deformations under uniaxial compression were examined, showing a high degree of agreement between experimental results and tetrapod simulations.

While the model provides a good qualitative description of viscoelastic damping, relaxation, and cyclic behavior, quantitative discrepancies remain, particularly with respect to the energy dissipation during (i) cyclic loading and (ii) stress relaxation. Specifically, our simulations consistently exhibit stronger damping and an earlier onset of plastic behavior than observed in the experiments. These deviations indicate limitations of the current model, suggesting future adaptations towards more complex interaction models between water and the alginate network.

The strategy for future applications of this simulation approach is a systematic, stepwise replacement of water with an organic liquid phase such as ethanol, which could also serve as a further validation step. Such experiments would allow testing whether the model remains predictive by adjusting the liquid-solid interaction parameters, while keeping tetrapod-tetrapod interaction parameters unchanged.

Beyond single-particle compression, the tetrapod DEM framework can be applied to multi-particle systems, such as packed beds of hydrogel particles (a scenario that is relevant during aerogel production). Thereby, utilizing key advantages of the DEM over other modeling approaches (e.g., continuum-based models), which are (i) excellent suitability for parallel computation and (ii) straightforward handling of inter-particle contacts.

Overall, the combination of experimental data and tetrapod-based simulations provides a robust framework for understanding and predicting the mechanical behavior of hydrogel particles. By capturing the interplay between particle geometry, viscoelasticity, and the biphasic structure of a gel, this approach establishes a foundation for process-relevant modeling of soft, deformable materials, including solvent exchange dynamics, and facilitates their scale-up to industrial applications.

CRediT authorship contribution statement

Lara Gibowsky: Writing – original draft, Methodology, Investigation, Formal analysis, Data curation, Conceptualization. **Lukas Maier:** Writing – original draft, Software, Methodology, Investigation, Formal analysis, Conceptualization. **Nanning Jaeschke:** Writing – original draft, Methodology, Formal analysis. **Irina Smirnova:** Writing – review & editing, Supervision, Funding acquisition, Conceptualization. **Stefan Radl:** Writing – review & editing, Supervision, Methodology, Conceptualization. **Pavel Gurikov:** Writing – review & editing, Supervision, Project administration, Methodology, Conceptualization.

Code availability

https://gitlab.tugraz.at/13097018C9D61E3C/LIGGGHTS-PUBLIC/tree/dev-Lukas_contactModel.

Declaration of competing interest

The authors declare the following financial interests/personal relationships which may be considered potential competing interests:

Lara Gibowsky reports financial support was provided by the German Research Foundation. Nanning Jaeschke reports financial support was provided by the German Research Foundation. Lara Gibowsky reports equipment, drugs, or supplies were provided by IFF Nutrition & Health GmbH& Co. KG. If there are other authors, they declare that they have no known competing financial interests or personal relationships that could have appeared to influence the work reported in this paper.

Acknowledgements

The authors acknowledge the use of high-performance computing resources (lcluster) provided by the ZID of Graz University of Technology. We gratefully acknowledge financial support from the German Research Foundation (DFG) through the Research Training Group GRK 2462 "Processes in Natural and Technical Particle-Fluid Systems" (PintPFS) and project number 572006271. The authors further thank IFF Nutrition & Health Germany GmbH & Co. KG (IFF Division Pharma Solutions, Walsrode-Bomlitz) for kindly providing the sodium alginate. This project was partially funded by the Deutsche Forschungsgemeinschaft (DFG, German Research Foundation) under SFB 1615 (Project-ID 503850735).

The authors gratefully acknowledge Swantje Pietsch and Amirali Khosrozadeh for insightful discussions on the mechanical characterization of individual particles, as well as Nicolas Castellanos Tolosa for experimental assistance.

Appendix A. Supplementary data

Supplementary data for this article can be found online at doi:10.1016/j.matdes.2026.116860.

Data availability

The dataset and associated Python scripts are available at: https://doi.org/10.15480/882.16495.

References

[1] G. Agarwal, J.H. Urrea-Quintero, H. Wessels, T. Wick, Parameter identification and uncertainty propagation of hydrogel coupled diffusion-deformation using POD-based reduced-order modeling, Comput. Mech. 75 (2025) 515–545. URL: https://doi.org/10.1007/s00466-024-02517-w, https://link.springer.com/10.1007/s00466-024-02517-w.

[2] C. Alves, L. Gibowsky, B. Schroeter, I. Smirnova, S. Heinrich, Simulation-based characterization of alginate aerogel packed bed compaction via DEM-BPM, Powder Technol. 460 (2025) 121048. URL: https://doi.org/10.1016/j.powtec.2025.121048, https://linkinghub.elsevier.com/retrieve/pii/S0032591025004437.

[3] S.T. Apuu, W. Hanif, D. Alsulaiman, N. Alcheikh, T.T. Truscott, Nondestructive determination of young's modulus of alginate hydrogels using a soft magnetorheological elastomer-based actuator, Mater. Des. 263 (2026) 115688, https://doi.org/10.1016/j.matdes.2026.115688

[4] A.D. Augst, H.J. Kong, D.J. Mooney, Alginate hydrogels as biomaterials, Macromol. Biosci. 6 (2006) 623–633. URL: https://doi.org/10.1002/mabi.200600069, https://onlinelibrary.wiley.com/doi/10.1002/mabi.200600069.

[5] S. Aygün, S. Klinge, Multiscale modeling of calcified hydrogel networks, PAMM 21 (2021) e202100115. URL: https://doi.org/10.1002/pamm.202100115, https://onlinelibrary.wiley.com/doi/10.1002/pamm.202100115.

[6] I. Ben Djemaa, F. Boulmedais, S. Auguste, M. Tarnowska, S. Andrieux, W. Drenckhan-Andreatta, Glucono-Delta-Lactone-Induced alginate gelation: new insights into the effect of the cross-linker carrier type on the hydrogel mechanics, Langmuir 40 (2024) 10492–10501. URL: https://doi.org/10.1021/acs.langmuir.3c03959, https://pubs.acs.org/doi/10.1021/acs.langmuir.3c03959.

[7] D.L. Blair, N.W. Mueggenburg, A.H. Marshall, H.M. Jaeger, S.R. Nagel, Force distributions in 3D granular assemblies: effects of packing order and inter-particle friction, Phys. Rev. E 63 (2001) 041304. URL: https://doi.org/10.1103/PhysRevE.63.041304, http://arxiv.org/abs/cond-mat/0009313.

[8] D. Caccavo, S. Cascone, G. Lamberti, A.A. Barba, Hydrogels: experimental characterization and mathematical modelling of their mechanical and diffusive behaviour, Chem. Soc. Rev. 47 (2018) 2357–2373. URL: https://doi.org/10.1039/C7CS00638A, https://xlink.rsc.org/?DOI=C7CS00638A.

[9] S. Cai, Y. Hu, X. Zhao, Z. Suo, Poroelasticity of a covalently crosslinked alginate hydrogel under compression, J. Appl. Phys. 108 (2010) 113514. URL: https://doi.org/10.1063/1.3517146, https://pubs.aip.org/jap/article/108/11/113514/372274/Poroelasticity-of-a-covalently-crosslinked.

[10] H.P.A. Calis, J. Nijenhuis, B.C. Paikert, F.M. Dautzenberg, CFD modelling and experimental validation of pressure drop and flow profile in a novel structured catalytic reactor packing, Chem. Eng. Sci. 56 (2001) 1713–1720.

[11] J. Canny, A computational approach to edge detection, IEEE Trans. Pattern Anal. Mach. Intell. (1986) 679–698. URL: https://doi.org/10.1109/TPAMI.1986.4767851, https://ieeexplore.ieee.org/document/4767851.

[12] R. Castillo-Acuna, D.M. Kochmann, Multiphysics modeling of hydrogels with a maximum-entropy-based meshless framework, Comput. Methods Appl. Mech. Eng. 446 (2025) 118293. URL: https://doi.org/10.1016/j.cma.2025.118293, https://linkinghub.elsevier.com/retrieve/pii/S0045782525005651.

[13] F.J. Castro, S. Radl, A combined SPH-DEM approach for extremely deformed granular packings: validation and compression tests, Comput. Part. Mech. 11 (2024) 185–196, https://doi.org/10.1007/s40571-023-00616-8

[14] E.S. Chan, T.K. Lim, W.P. Voo, R. Pogaku, B.T. Tey, Z. Zhang, Effect of formulation of alginate beads on their mechanical behavior and stiffness, Particuology 9 (2011) 228–234. URL: https://doi.org/10.1016/j.partic.2010.12.002, https://linkinghub.elsevier.com/retrieve/pii/S1674200111000563.

[15] Y. Chu, L. Huang, W. Hao, T. Zhao, H. Zhao, W. Yang, X. Xie, L. Qian, Y. Chen, J. Dai, Long-term stability, high strength, and 3D printable alginate hydrogel for cartilage tissue engineering application, Biomed. Mater. 16 (2021) 064102. URL: https://doi.org/10.1088/1748-605X/ac2595, https://iopscience.iop.org/article/10.1088/1748-605X/ac2595.

[16] J.T. Clemmer, J.M. Monti, J.B. Lechman, A soft departure from jamming: the compaction of deformable granular matter under high pressures, Soft Matter 20 (2024) 1702–1718. URL: https://doi.org/10.1039/D3SM01373A, https://xlink.rsc.org/?DOI=D3SM01373A.

[17] M. Czerner, L.S. Fellay, M.P. Suárez, P.M. Frontini, L.A. Fasce, Determination of elastic modulus of gelatin gels by indentation experiments, Procedia Mater. Sci. 8 (2015) 287–296. URL: https://doi.org/10.1016/j.mspro.2015.04.075, https://linkinghub.elsevier.com/retrieve/pii/S2211812815000760.

[18] P.N. Depta, P. Gurikov, B. Schroeter, A. Forgács, J. Kalmár, G. Paul, L. Marchese, S. Heinrich, M. Dosta, DEM-based approach for the modeling of gelation and its application to alginate, J. Chem. Inf. Model. 62 (2022) 49–70, https://doi.org/10.1021/acs.jcim.1c01076, https://pubs.acs.org/doi/10.1021/acs.jcim.1c01076.

[19] M.P. Dirauf, A. Hajnal, P. Gurikov, A.S. Braeuer, Protein gel shrinkage during solvent exchange: quantification of gel compaction, mass transfer and compressive strength, Food Hydrocoll. 120 (2021) 106916. URL: https://doi.org/10.1016/j.foodhyd.2021.106916, https://linkinghub.elsevier.com/retrieve/pii/S0268005X21003325.

[20] M. Dorn, D. Hekmat, Simulation of the dynamic packing behavior of preparative chromatography columns via discrete particle modeling, Biotechnol. Prog. 32 (2016) 363–371. URL: https://doi.org/10.1002/btpr.2210, https://aiche.onlinelibrary.wiley.com/doi/10.1002/btpr.2210.

[21] M. Dosta, K. Jarolin, P. Gurikov, Modelling of mechanical behavior of biopolymer alginate aerogels using the bonded-particle model, Molecules 24 (2019) 2543. URL: https://doi.org/10.3390/molecules24142543, https://www.mdpi.com/1420-3049/24/14/2543.

[22] K.M. Eckert, J. Bonsen, A. Hajnal, J. Gmeiner, J. Hasse, M. Adrian, J. Karsten, P.A. Kißling, A. Penn, B. Fiedler, G.A. Luinstra, I. Smirnova, Enhancing swelling kinetics of pNIPAM lyogels: the role of crosslinking, copolymerization, and solvent, Fluid Ph. Equilibria 597 (2025) 114462. URL: https://doi.org/10.1016/j.fluid.2025.114462, https://linkinghub.elsevier.com/retrieve/pii/S0378381225001323.

[23] A. Ed-Daoui, N. Chafi, F. Khoshnaw, M. Benelmostafa, M. Dahmani, M. Benaichi, A. El Haimeur, M. Hammi, Unveiling the poroelastic evolution of Agar hydrogels through the drying process, Sci. Rep. 16 (2026) 11929. URL: https://doi.org/10.1038/s41598-026-41283-y, https://www.nature.com/articles/s41598-026-41283-y.

[24] A. Ed-Daoui, P. Snabre, Poroviscoelasticity and compression-softening of agarose hydrogels, Rheol. Acta 60 (2021) 327–351. URL: https://doi.org/10.1007/s00397-021-01267-3, https://link.springer.com/10.1007/s00397-021-01267-3.

[25] R.D. Egholm, S.F. Christensen, P. Szabo, Stress–strain behavior in uniaxial compression of polymer gel beads, J. Appl. Polym. Sci. 102 (2006) 3037–3047, https://doi.org/10.1002/app.24715, https://onlinelibrary.wiley.com/doi/10.1002/app.24715.

[26] P.A. Galie, R.L. Spilker, J.P. Stegemann, A linear, biphasic model incorporating a brinkman term to describe the mechanics of cell-seeded collagen hydrogels, Ann. Biomed. Eng. 39 (2011) 2767–2779, https://doi.org/10.1007/s10439-011-0371-9

[27] F. Gomollón-Bel, IUPAC top ten emerging technologies in chemistry 2022, Chem. Int. 44 (2022).

[28] P. Gurikov, S.P. Raman, D. Weinrich, M. Fricke, I. Smirnova, A novel approach to alginate aerogels: carbon dioxide induced gelation, RSC Adv. 5 (2015) 7812–7818. URL: https://doi.org/10.1039/C4RA14653K, https://xlink.rsc.org/?DOI=C4RA14653K.

[29] M. Haustein, A. Gladkyy, R. Schwarze, Discrete element modeling of deformable particles in YADE, Softwarex 6 (2017) 118–123. URL: https://doi.org/10.1016/j.softx.2017.05.001, https://linkinghub.elsevier.com/retrieve/pii/S2352711017300134.

[30] D. Heikens, S.D. Sjoerdsma, W.J. Coumans, A mathematical relation between volume strain, elongational strain and stress in homogeneous deformation, J. Mater. Sci. 16 (1981) 429–432. URL: https://doi.org/10.1007/BF00738633, http://link.springer.com/10.1007/BF00738633.

[31] H. Hertz, Über die berührung fester elastischer körper, J. Reine Angew. Math. 92 (1881) 156–171.

[32] S. Hirotsu, Some exotic properties of polymer gels associated with the volume phase transition, Ferroelectrics 203 (1997) 375–388. URL: https://doi.org/10.1080/00150199708012861, http://www.tandfonline.com/doi/abs/10.1080/00150199708012861.

[33] T.C. Ho, C.C. Chang, H.P. Chan, T.W. Chung, C.W. Shu, K.P. Chuang, T.H. Duh, M.H. Yang, Y.C. Tyan, Hydrogels: properties and applications in biomedicine, Molecules 27 (2022) 2902. URL: https://doi.org/10.3390/molecules27092902, https://www.mdpi.com/1420-3049/27/9/2902.

[34] X. Hu, J. Karnetzke, M. Fassbender, S. Drücker, S. Bettermann, B. Schroeter, W. Pauer, H.U. Moritz, B. Fiedler, G. Luinstra, I. Smirnova, Smart reactors – combining stimuli-responsive hydrogels and 3D printing, Chem. Eng. J. 387 (2020) 123413. URL: https://doi.org/10.1016/j.cej.2019.123413, https://linkinghub.elsevier.com/retrieve/pii/S1385894719328268.

[35] F. Irgens, Continuum Mechanics, Springer, Berlin Heidelberg, Berlin, Heidelberg, 2008, https://doi.org/10.1007/978-3-540-74298-2

[36] S. Ishwarya, P, R, S, P. Nisha, Advances and prospects in the food applications of pectin hydrogels, Crit. Rev. Food Sci. Nutr. 62 (2022) 4393–4417, https://doi.org/10.1080/10408398.2021.1875394, https://www.tandfonline.com/doi/full/10.1080/10408398.2021.1875394.

[37] K. Iwashita, M. Oda, Rolling resistance at contacts in simulation of shear band development by DEM, J. Eng. Mech. 124 (1998) 285–292. URL: https://doi.org/10.1061/(ASCE)0733-9399(1998)124:3(285), https://ascelibrary.org/doi/10.1061/%28ASCE%290733-9399%281998%29124%3A3%28285%29.

[38] L.C. Johnson, R.N. Zia, E. Moghimi, G. Petekidis, Influence of structure on the linear response rheology of colloidal gels, J. Rheol. 63 (2019) 583–608. URL: https://doi.org/10.1122/1.5082796, https://pubs.aip.org/jor/article/63/4/583/922638/Influence-of-structure-on-the-linear-response.

[39] T. Johnson, F. Iacoviello, D. Hayden, J. Welsh, P. Levison, P. Shearing, D. Bracewell, Packed bed compression visualisation and flow simulation using an erosion-dilation approach, J. Chromatogr. A 1611 (2020) 460601. URL: https://doi.org/10.1016/j.chroma.2019.460601, https://linkinghub.elsevier.com/retrieve/pii/S002196731931009X.

[40] C.J. Kitrick, A unified approach to class I, II & III geodesic domes, Int. J. Space Struct. 5 (1990) 223–246, https://doi.org/10.1177/026635119000500307

[41] C. Kloss, C. Goniva, A. Hager, S. Amberger, S. Pirker, Models, algorithms and validation for opensource DEM and CFD-DEM. progress in computational fluid dynamics, An Int. J. 12 (2012) 140. URL: https://doi.org/10.1504/PCFD.2012.047457, http://www.inderscience.com/link.php?id=47457.

[42] C.K. Kuo, P.X. Ma, Maintaining dimensions and mechanical properties of ionically crosslinked alginate hydrogel scaffolds *in vitro*, J. Biomed. Mater. Res. A 84A (2008) 899–907, https://doi.org/10.1002/jbm.a.31375, https://onlinelibrary.wiley.com/doi/10.1002/jbm.a.31375.

[43] J. Lei, Z. Li, S. Xu, Z. Liu, Recent advances of hydrogel network models for studies on mechanical behaviors, Acta Mech. Sin. 37 (2021) 367–386. URL: https://

doi.org/10.1007/s10409-021-01058-2, https://link.springer.com/10.1007/s10409-021-01058-2.
[44] J. Lei, S. Xu, Z. Li, Z. Liu, Study on large deformation behavior of polyacrylamide hydrogel using dissipative particle dynamics, Front. Chem. 8 (2020) 115. URL: https://doi.org/10.3389/fchem.2020.00115, https://www.frontiersin.org/article/10.3389/fchem.2020.00115/full.
[45] L. Li, Z. Liu, R. Qi, Molecular dynamics simulations in hydrogel research and its applications in energy utilization: a review, Energy Rev. 3 (2024) 100072. URL: https://doi.org/10.1016/j.enrev.2024.100072, https://linkinghub.elsevier.com/retrieve/pii/S2772970224000051.
[46] F. Liu, D. Wu, W. Hong, Mechanism study on mechanical properties of physical–chemical hybrid hydrogels by coarse-grained molecular dynamics simulations, ACS Appl. Polym. Mater. 5 (2023) 1707–1714. URL: https://doi.org/10.1021/acsapm.2c01681, https://pubs.acs.org/doi/10.1021/acsapm.2c01681.
[47] P. Loidolt, M.H. Ulz, J. Khinast, Modeling yield properties of compacted powder using a multi-particle finite element model with cohesive contacts, Powder Technol. 336 (2018) 426–440. URL: https://doi.org/10.1016/j.powtec.2018.06.018, https://linkinghub.elsevier.com/retrieve/pii/S003259101830456X.
[48] L. Maier, M. Mitterlindner, H. Benabchiasli, G. Fasching, S. Radl, The uncertainty inherent to DEM simulations of interlocking particles, Sci. Rep. 15 (2025) 7599. URL: https://doi.org/10.1038/s41598-025-90129-6, https://www.nature.com/articles/s41598-025-90129-6.
[49] M. Mascara, C. Shakya, S. Radl, A. Mayrhofer, C. Kloss, A viscoelastic bonded particle model to predict rheology and mechanical properties of hydrogel spheres, Granul. Matter 26 (2024) 64. URL: https://doi.org/10.1007/s10035-024-01429-z, https://link.springer.com/10.1007/s10035-024-01429-z.
[50] V.C. Mow, S.C. Kuei, W.M. Lai, C.G. Armstrong, Biphasic creep and stress relaxation of articular cartilage in compression: theory and experiments, J. Biomech. Eng. 102 (1980) 73–84. URL: https://doi.org/10.1115/1.3138202, https://dx.doi.org/10.1115/1.3138202.
[51] V. Nguyen, C. Wang, C. Thomas, Z. Zhang, Mechanical properties of single alginate microspheres determined by microcompression and finite element modelling, Chem. Eng. Sci. 64 (2009) 821–829. URL: https://doi.org/10.1016/j.ces.2008.10.050, https://linkinghub.elsevier.com/retrieve/pii/S0009250908005988.
[52] S. Nikolov, Modeling and Application of Polymeric Microgels (Ph.D. thesis), Institute of Technology, Georgia, 2020.
[53] N. Otsu, A threshold selection method from gray-level histograms, IEEE Trans. Syst. Man Cybern. 9 (1979) 62–66. URL: https://doi.org/10.1109/TSMC.1979.4310076, http://ieeexplore.ieee.org/document/4310076/.
[54] C. Ouwerx, N. Velings, M. Mestdagh, M. Axelos, Physico-chemical properties and rheology of alginate gel beads formed with various divalent cations, Polym. Gels Netw. 6 (1998) 393–408. URL: https://doi.org/10.1016/s0966-7822(98)00035-5, https://linkinghub.elsevier.com/retrieve/pii/S0966782298000355.
[55] M.T.J.J.M. Punter, B.E. Vos, B.M. Mulder, G.H. Koenderink, Poroelasticity of (bio)polymer networks during compression: theory and experiment. URL: 2019, https://doi.org/10.48550/arXiv.1910.00490, http://arxiv.org/abs/1910.00490.
[56] S. Radl, Parcel methods for cohesive and interlocking granular materials, 2025, Barcelona. URL: https://congressarchive.cimne.com/particles_2025/assets/radl_parcelmethodscohesiveinterlocking.pdf.
[57] S. Radl, H. Benabchiasli, G. Fasching, M. Mitterlindner, M.S. Salehi, How CFD-DEM simulations benefit from machine learning, in: Proceedings of the 14th European Conference on Industrial Furnaces and Boilers, 2024.
[58] A. Rege, M. Hillgärtner, M. Itskov, Mechanics of biopolymer aerogels based on microstructures generated from 2-d voronoi tessellations, J. Supercrit. Fluids 151 (2019) 24–29. URL: https://doi.org/10.1016/j.supflu.2019.04.018, https://linkinghub.elsevier.com/retrieve/pii/S0896844618308684.
[59] W. Reynolds, M. Conrad, S. Mbeukem, R. Stank, I. Smirnova, Pressure drop, mechanic deformation, stabilization and scale-up of wheat straw fixed-beds during hydrothermal pretreatment: experiments and modeling, Chem. Eng. J. 360 (2019) 1587–1600. URL: https://doi.org/10.1016/j.cej.2018.11.001, https://linkinghub.elsevier.com/retrieve/pii/S1385894718322010.
[60] N.R. Richbourg, M.K. Rausch, N.A. Peppas, Cross-evaluation of stiffness measurement methods for hydrogels, Polymer 258 (2022) 125316. URL: https://doi.org/10.1016/j.polymer.2022.125316, https://linkinghub.elsevier.com/retrieve/pii/S0032386122008035.
[61] M. Robitzer, L. David, C. Rochas, F. Di Renzo, F. Quignard, Nanostructure of calcium alginate aerogels obtained from multistep solvent exchange route, Langmuir 24 (2008) 12547–12552. URL: https://doi.org/10.1021/la802103t, https://pubs.acs.org/doi/10.1021/la802103t.
[62] J. Rojek, S. Nosewicz, K. Thoeni, 3D formulation of the deformable discrete element method, Int. J. Numer. Methods Eng. 122 (2021) 3335–3367, https://doi.org/10.1002/nme.6666, https://onlinelibrary.wiley.com/doi/10.1002/nme.6666.
[63] A. Román-Guerrero, S. Cortés-Camargo, E. Alpizar-Reyes, M.F. Fabela-Morón, J. Cruz-Olivares, S.K. Velázquez-Gutiérrez, C. Pérez-Alonso, Chemically modified alginate-based hydrogel-matrices in drug delivery, Macromol 5 (36. URL: 2025), https://doi.org/10.3390/macromol5030036, https://www.mdpi.com/2673-6209/5/3/36.
[64] S.S. Sandha, M. Aggarwal, I. Fedorov, M. Srivastava, MANGO: a Python library for parallel hyperparameter tuning. URL: 2020, https://doi.org/10.48550/arXiv.2005.11394, http://arxiv.org/abs/2005.11394.
[65] S.S. Sandha, M. Aggarwal, S.S. Saha, M. Srivastava, Enabling hyperparameter tuning of machine learning classifiers in production, in: 2021 IEEE Third International Conference on Cognitive Machine Intelligence (CogMI), IEEE, Atlanta, GA, USA, 2021, pp. 262–271. URL: https://doi.org/10.1109/CogMI52975.2021.00041, https://ieeexplore.ieee.org/document/9750322/.
[66] M. Santhamoorthy, S.C. Kim, A review of the development of biopolymer hydrogel-based scaffold materials for drug delivery and tissue engineering applications, Gels 11 (2025) 178. URL: https://doi.org/10.3390/gels11030178, https://www.mdpi.com/2310-2861/11/3/178.
[67] J. Schindelin, I. Arganda-Carreras, E. Frise, V. Kaynig, M. Longair, T. Pietzsch, S. Preibisch, C. Rueden, S. Saalfeld, B. Schmid, J.Y. Tinevez, D.J. White, V. Hartenstein, K. Eliceiri, P. Tomancak, A. Cardona, Fiji: an open-source platform for biological-image analysis, Nat. Methods 9 (2012) 676–682, https://doi.org/10.1038/nmeth.2019, https://www.nature.com/articles/nmeth.2019.
[68] I. Selmer, A.S. Behnecke, J. Quiño, A.S. Braeuer, P. Gurikov, I. Smirnova, Model development for SC-drying kinetics of aerogels: Part 1. monoliths and single particles, J. Supercrit. Fluids 140 (2018) 415–430. URL: https://doi.org/10.1016/j.supflu.2018.07.002, https://linkinghub.elsevier.com/retrieve/pii/S0896844618302766.
[69] D.P.F. Silva, R.C.V. Coelho, I. Pagonabarraga, S. Succi, M.M. Telo Da Gama, N.A.M. Araújo, Lattice Boltzmann simulation of deformable fluid-filled bodies: progress and perspectives, Soft Matter 20 (2024) 2419–2441. URL: https://doi.org/10.1039/D3SM01648J, https://xlink.rsc.org/?DOI=D3SM01648J.
[70] D. Stadlthanner, G. Leitner, C. Landschützer, Parametrization of a simulation model for flexible small consignments using parallel Bayesian optimization, Logist. J.: Proc. (2024). https://doi.org/10.2195/LJ_PROC_STADLTHANNER_EN_202410_01, URL: https://proc.logistics-journal.de/article/view/1103.
[71] C. Thornton, C.W. Randall, Applications of theoretical contact mechanics to solid particle system simulation, In M. Satake, J.T. Jenkins (Eds.), Studies in Applied Mechanics, vol. 20 of Micromechanics of Granular Materials, pp. Elsevier, 1988, pp. 133–142. URL: https://doi.org/10.1016/B978-0-444-70523-5.50023-0, https://www.sciencedirect.com/science/article/pii/B9780444705235500230.
[72] S. Todros, M. Castilho, D.M. Espino, P.G. Pavan, Editorial: mechanical behavior of hydrogels for soft tissue replacement and regeneration, Front. Bioeng. Biotechnol. 11 (2023) 1254076. URL: https://doi.org/10.3389/fbioe.2023.1254076, https://www.frontiersin.org/articles/10.3389/fbioe.2023.1254076/full.
[73] N. Tomovic, K. Trifkovic, M. Rakin, M. Rakin, B. Bugarski, Influence of compression speed and deformation percentage on mechanical properties of calcium alginate particles, Chem. Ind. Chem. Eng. Q. 21 (2015) 411–417. URL: https://doi.org/10.2298/ciceq140228043t, https://doiserbia.nb.rs/Article.aspx?ID=1451-93721400043T.
[74] J.H. Urrea-Quintero, M. Marino, T. Wick, U. Nackenhorst, A comparative analysis of transient finite-strain coupled diffusion-deformation theories for hydrogels, Arch. Comput. Methods Eng. (2024), https://doi.org/10.1007/s11831-024-10101-x, https://link.springer.com/10.1007/s11831-024-10101-x.
[75] C. Wang, C. Cowen, Z. Zhang, C. Thomas, High-speed compression of single alginate microspheres, Chem. Eng. Sci. 60 (2005) 6649–6657. URL: https://doi.org/10.1016/j.ces.2005.05.052, https://linkinghub.elsevier.com/retrieve/pii/S0009250905005026.
[76] R. Yang, T. Gao, D. Li, H. Liang, Q. Xu, Simulation of fracture behaviour of hydrogel by discrete element method, Micro Nano Lett. 13 (2018) 743–746. URL: https://doi.org/10.1049/mnl.2017.0844, https://ietresearch.onlinelibrary.wiley.com/doi/10.1049/mnl.2017.0844.
[77] H. You, S. Zheng, K. Lam, H. Li, Heterogeneous hydrogel fracture simulation study using community detection, Int. J. Mech. Sci. 286 (2025) 109848. URL: https://doi.org/10.1016/j.ijmecsci.2024.109848, https://linkinghub.elsevier.com/retrieve/pii/S0020740324008890.
[78] X. Zeng, Y. Yang, W. Liu, C. Wen, R. Qiu, J. Pang, S. Wu, Real-time quantitative measurement of mechanical properties of spherical hydrogels during degradation by hydrodynamic loading and numerical simulation, Polym. Degrad. Stab. 202 (2022) 110055. URL: https://doi.org/10.1016/j.polymdegradstab.2022.110055, https://linkinghub.elsevier.com/retrieve/pii/S0141391022002336.
[79] Y. Zhang, K. Xu, Y. Bai, L. Tang, Z. Jiang, Y. Liu, Z. Liu, L. Zhou, X. Zhou, Features of the volume change and a new constitutive equation of hydrogels under uniaxial compression, J. Mech. Behav. Biomed. Mater. 85 (2018) 181–187. URL: https://doi.org/10.1016/j.jmbbm.2018.06.004, https://linkinghub.elsevier.com/retrieve/pii/S1751616118306453.
[80] L. Zhao, Z. Zhang, Mechanical characterization of biocompatible microspheres and microcapsules by direct compression, Artif. Cells Nanomed. Biotechnol. 32 (2004) 25–40. URL: https://doi.org/10.1081/BIO-120028666, http://www.tandfonline.com/doi/full/10.1081/BIO-120028666.
[81] S. Zhao, W.J. Malfait, N. Guerrero-Alburquerque, M.M. Koebel, G. Nyström, Biopolymer-aerogele und -schäume: chemie, eigenschaften und anwendungen, Angew. Chem. 130 (2018) 7704–7733. URL: https://doi.org/10.1002/ange.201709014, https://onlinelibrary.wiley.com/doi/10.1002/ange.201709014.
[82] S. Zhao, X. Zhou, W. Liu, C. Lai, Random packing of tetrahedral particles using the polyhedral discrete element method, Particuology 23 (2015) 109–117. URL: https://doi.org/10.1016/j.partic.2015.02.007, https://linkinghub.elsevier.com/retrieve/pii/S1674200115001224.
[83] Q. Zhou, C.P. Chng, Y. Zhao, Y. Wang, H. Xu, Y. Huo, C. Huang, Ethanol-induced gelation enables direct three-dimensional printing of sodium alginate hydrogel, Mater. Des. 239 (2024) 112746, https://doi.org/10.1016/j.matdes.2024.112746
[84] W. Zunker, S. Dunatunga, S. Thakur, P. Tang, K. Kamrin, Experimentally validated DEM for large deformation powder compaction: mechanically-derived contact model and screening of non-physical contacts, Powder Technol. 459 (2025) 120972. URL: https://doi.org/10.1016/j.powtec.2025.120972, https://linkinghub.elsevier.com/retrieve/pii/S0032591025003675.